

Robust Modality-Incomplete Anomaly Detection: a Modality-Instructive Framework with Benchmark

Bingchen Miao

miaobingchen23@zju.edu.cn

Zhejiang University

Hangzhou, Zhejiang, China

Wangyu Wu

v11dryad@foxmail.com

University of Liverpool

Liverpool, England

Haochen Shi

haochen.shi@umontreal.ca

Université de Montréal

Montréal, Canada

Wenqiao Zhang*

wenqiaozhang@zju.edu.cn

Zhejiang University

Hangzhou, Zhejiang, China

Siliang Tang

siliang@zju.edu.cn

Zhejiang University

Hangzhou, Zhejiang, China

Jun Xiao

junx@cs.zju.edu.cn

Zhejiang University

Hangzhou, Zhejiang, China

Juncheng Li*

junchengli@zju.edu.cn

Zhejiang University

Hangzhou, Zhejiang, China

Zhaocheng Li

3200106072@zju.edu.cn

Zhejiang University

Hangzhou, Zhejiang, China

Yuetong Zhuang

yzhuang@zju.edu.cn

Zhejiang University

Hangzhou, Zhejiang, China

Abstract

Multimodal Industrial Anomaly Detection (MIAD)—fusing 3D point clouds and 2D RGB for product defect detection—is critical to quality inspection. However, existing MIAD methods assume all modalities are available and paired, overlooking real-scenario modality-missing and risking overfitting to incomplete data. To address these, we conduct the first comprehensive study on **Modality-Incomplete Industrial Anomaly Detection (MIIAD)** and establish **MIIAD Bench**, a benchmark covering diverse missing settings. Meanwhile, we propose **RADAR**, a robust two-stage **Robust modality-instructive fusing and Detecting frAmewoRk**. **RADAR** integrates **i**) a Modality-Incomplete Instruction mechanism—guiding the multimodal Transformer to focus more on available modal info, and **ii**) a Double-Pseudo Hybrid Module to highlight unique modality combinations and reduce overfitting. Our results show **RADAR** outperforms prior methods markedly on **MIIAD Bench**.

CCS Concepts

- Computing methodologies → Computer vision problems.

Keywords

Industrial Anomaly Detection, Modality-Incomplete Learning

ACM Reference Format:

Bingchen Miao, Wenqiao Zhang, Juncheng Li, Wangyu Wu, Siliang Tang, Zhaocheng Li, Haochen Shi, Jun Xiao, and Yuetong Zhuang. 2025. Robust

*Corresponding Author.

Permission to make digital or hard copies of all or part of this work for personal or classroom use is granted without fee provided that copies are not made or distributed for profit or commercial advantage and that copies bear this notice and the full citation on the first page. Copyrights for components of this work owned by others than the author(s) must be honored. Abstracting with credit is permitted. To copy otherwise, or republish, to post on servers or to redistribute to lists, requires prior specific permission and/or a fee. Request permissions from permissions@acm.org.

MM '25, Dublin, Ireland

© 2025 Copyright held by the owner/author(s). Publication rights licensed to ACM.

ACM ISBN 979-8-4007-2035-2/2025/10

<https://doi.org/10.1145/3746027.3754766>

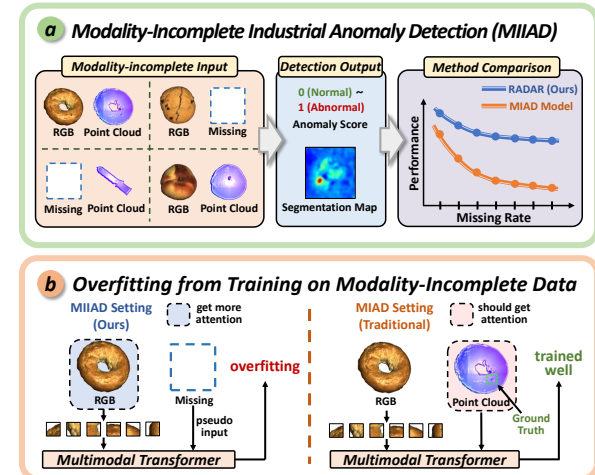


Figure 1: (a). Outline of MIIAD. MIIAD processes modality-incomplete data, generating anomaly scores and segmentation maps. Our model RADAR surpasses most MIAD methods on this task. (b). Overfitting from modality-incomplete training. Training with incomplete-modal data can cause the model to focus on irrelevant features, leading to overfitting.

Modality-Incomplete Anomaly Detection: a Modality-Instructive Framework with Benchmark. In *Proceedings of the 33rd ACM International Conference on Multimedia (MM '25, October 27–31, 2025, Dublin, Ireland. ACM, New York, NY, USA, 18 pages. <https://doi.org/10.1145/3746027.3754766>*

1 Introduction

Industrial Anomaly Detection (IAD) is pivotal in industrial quality inspection, focusing on product defects [15, 37]. Recent studies [45] emphasize 3D geometries and color characteristics in defect identification, suggesting systems integrating 3D point clouds with 2D images represent a promising method. In recent years, emerging multimodal Transformer-based methods [46, 50] provide solutions for Multimodal Industrial Anomaly Detection (MIAD).

However, previous MIAD work typically assumes complete data availability [30], an assumption rarely feasible in industrial environments due to equipment limitations and privacy concerns, particularly with 3D data acquisition [41]. Recent studies [23, 47] have emphasized that exploring the issue of modality-incompleteness, including corresponding benchmark and solution research, is meaningful and practical. To bridge the gap, we first introduce a novel and challenging task: **Modality-Incomplete Industrial Anomaly Detection (MIIAD)**. And to support this, we propose a comprehensive benchmark, **MIIAD Bench**, which collects multimodal industrial anomaly datasets from MVTec-3D AD [4] and Eyecandies [6] datasets, and constructs primary 30%, 50%, and 70% modality-missing data splits under the guidance of experts in industrial anomaly detection. This benchmark aims to simulate various missing-modality scenarios that may occur in data samples, such as accessing only 2D RGB images or 3D point clouds during training or testing phases. To our knowledge, we are the first to systematically propose the MIIAD task and provide a benchmark with rich, expert-guided data splits. We look forward to contributing to the advancement of MIAD.

With our new benchmark, we evaluate state-of-the-art (SOTA) MIAD models and identify key limitations: **i) Lack of robustness to varying modality-missing scenarios**: Unsurprisingly, as shown in Fig. 1 a, SOTA models suffer sharp performance drops, revealing struggles with MIIAD. Modality absence (at any rate, training/testing) creates diverse incomplete scenarios [23], yet even advanced missing-modality methods [41, 44] fail to boost MIAD performance on **MIIAD Bench**. This highlights the urgent need for robust IAD methods adaptable to incomplete modalities. **ii) Overfitting from training on modality-incomplete data**: Additionally, training on such data risks overfitting [57]; e.g., single-modal data struggles to support some tasks, leading models to overfit irrelevant features. As in Fig. 1 b, models learning from anomaly-unidentifiable 2D data focus more on irrelevant features, causing overfitting. This demands methods robust to distinguishing different modality combinations and mitigating overfitting.

To facilitate robust detection in such an imperfect environment, we propose **RADAR**, a **R**obust mod**A**lity-instructive fusing and **D**etecting fr**A**mewo**R**k. It enhances the model's ability to handle incomplete modalities in both the feature fusion and anomaly detection stages, comprising two main components: **i) Stage1: Adaptive Instruction Fusion**: In the feature fusion, we treat modality-complete and modality-incomplete scenarios as different inputs, constructing modality-incomplete instructions based on prompt-learning. These instructions guide the multimodal Transformer to robustly adapt to various modality-incomplete scenarios through trainable parameters. We also propose a Adaptive Learning Module based on HyperNetwork to dynamically adjust the parameters of the multimodal Transformer. **ii) Stage2: Double-Pseudo Hybrid Detection**: To mitigate overfitting issues caused by missing modality data, we design a Double-Pseudo Hybrid Module in the anomaly detection. This module employs a double-head structure with different supervision to highlight the uniqueness of different modality combinations, enabling the model to better focus on features that can complete the anomaly detection task. Finally, we integrate features stored in three repositories and make decisions based on the Mahalanobis Distance Matrix (MDM) and One-Class Support Vector Machine (OCSVM).

Extensive experiments demonstrate broad value of our work: **i) Introducing a challenging practical new task**: Recent advanced MIAD methods struggle significantly on our proposed **MIIAD Bench**. For instance, Shape-Guided [8] M3DM [45] show at least 3% metric degradation in the 30% split compared to the modality-complete setting, and at least 16% degradation at 70% missing rate. Meanwhile, missing-modality based methods provide merely 1% improvement over baselines. This confirms MIIAD's substantial challenge practical value. **ii) Improving existing advanced MIAD methods**: Conversely, our **RADAR** model achieves SOTA performance on **MIIAD Bench**, outperforming the M3DM baseline by at least 3% and 5% at 30% and 70% missing rates respectively across all metrics. This validates our two-stage framework's effectiveness. **iii) Outperforming other missing-modality based methods**: We significantly surpass missing-modality approaches, achieving at least 4% higher metrics at 70% missing rate, demonstrating our framework's broad applicability for modality-missing scenarios.

Our contributions are threefold:

- We propose a new challenging and practical task: **Modality-Incomplete Industrial Anomaly Detection (MIIAD)**, and design a new benchmark, **MIIAD Bench**.
- We propose an end-to-end MIIAD learning framework, called **RADAR**, which enhances the robustness of the multimodal Transformer in a modality-incomplete setting.
- Experiments demonstrate that, through modality-incomplete instruction and Double-Pseudo structure training, our framework significantly outperforms other methods in MIIAD.

2 Related Work

2.1 Industrial Anomaly Detection

2D Industrial Anomaly Detection can be divided into: **i) Feature Extraction Methods**: Approaches such as teacher-student architecture [3, 39] and one-class classification (OCC) [20, 58] leverage pre-trained models or hypersphere-based strategies to distinguish anomalies. **ii) Reconstruction-based Methods**: These use encoders and decoders to reconstruct images for pixel-level anomaly detection, including autoencoders [9], GANs [27, 40], transformers [21], and diffusion models [49].

3D Industrial Anomaly Detection offers advantages in capturing spatial information beyond what is available in RGB images. The release of the MVTec 3D-AD dataset [2] has spurred several papers focusing on anomaly detection in 3D industrial images. Bergmann and Sattlegger [5] introduced a teacher-student model for 3D anomaly detection, while Horwitz and Hoshen [19] proposed a method that combines hand-crafted 3D representations with 2D features.

2.2 Modality-Incomplete Learning

Variational auto-encoders [43] effectively generate missing modalities unsupervised, but they typically overlook crucial shared vs. modality-specific feature distinctions [44]. Robust-Mseg [7] addresses this by disentangling features into modality-specific appearance codes and modality-invariant content codes. SMIL [31] achieves flexible incomplete data handling through Bayesian meta-learning, while ShaSpec [44] offers a simpler yet effective architecture for multi-task learning. We follow these works' modality-missing settings to ensure method generality.

Compared with these methods with a single feature fusion stage, our method contains two stages to enhance the model's robustness.

Table 1: MIIAD Bench - MVTec-3D AD Split with different missing types and rates.

Missing Rate	Type	3D PC in # Train	2D RGB in # Train	3D PC in # Test	2D RGB in # Test
30%	3D PC	1860	2656	840	1197
	2D RGB	2656	1860	1197	840
	Both	2260	2260	1020	1020
50%	3D PC	1330	2656	600	1197
	2D RGB	2656	1330	1197	600
	Both	1990	1990	900	900
70%	3D PC	800	2656	360	1197
	2D RGB	2656	800	1197	360
	Both	1730	1730	780	780

3 MIIAD

3.1 Problem Formulation

To systematically benchmark the robustness of current methods for industrial anomaly detection under modality-incomplete scenarios, we introduce a novel task called **Modality-Incomplete Industrial Anomaly Detection (MIIAD)**. MIIAD aims to assess model performance for industrial anomaly detection in diverse and complex modality-missing scenarios. We consider MIIAD tasks involving two modalities: 2D RGB image and 3D point cloud. Specifically, a MIIAD dataset, denoted as \mathcal{D} , can be formally divided into three subsets based on the modality missing situations: $\mathcal{D} = \{\mathcal{D}^C, \mathcal{D}^{2D}, \mathcal{D}^{3D}\}$. Here, $\mathcal{D}^C = \{(x_i^{2D}, x_i^{3D}, y_i)\}$ ($i \in 1, \dots, |\mathcal{D}^C|$) represents the modality-complete subset, $\mathcal{D}^{2D} = \{(x_i^{2D}, y_i)\}$ ($i \in 1, \dots, |\mathcal{D}^{2D}|$) comprises samples missing 3D point clouds, and $\mathcal{D}^{3D} = \{(x_i^{3D}, y_i)\}$ ($i \in 1, \dots, |\mathcal{D}^{3D}|$) includes samples lacking 2D RGB images. The primary task objective is to effectively perform IAD in various modality-incomplete settings.

3.2 MIIAD Bench

Dataset Construction. To cater to our research on modality-incomplete in IAD, we reconstructed the two prevailing datasets MVTec-3D AD [4] and Eyecandies [6] into a modality-incomplete setting, called **MIIAD Bench**, as shown in the upper part of Fig. 2, guided by domain experts. In **MIIAD Bench**, modality incompleteness may occur in either training or testing phases, with varying missing rates. The details of main data splits are shown in Tab. 1 and Tab. 2.

For a comprehensive study, we primarily set modality missing rates at 30%, 50%, and 70% for three scenarios: 3D point cloud missing, RGB missing, and dual-modality missing. This aligns with prior work [1, 35, 44, 54] on modality missing settings and is recognized by our consulted domain experts. We employed a random sampler to construct data covering three types of modality incompleteness: 3D point cloud modality-incomplete, 2D RGB image modality-incomplete, or both modalities-incomplete. For the first two scenarios, setting the missing rate of 3D point cloud data to $\eta\%$ implies the data comprises solely 2D RGB images of $\eta\%$ and complete data of $(1 - \eta)\%$. Conversely, when the missing rate of 2D RGB image data is $\eta\%$, the situation is reversed. In cases where both modalities are incomplete with a missing rate of $\eta\%$, the data includes $\frac{\eta}{2}\%$ 2D RGB image data, $\frac{\eta}{2}\%$ 3D point cloud data, and $(1 - \eta)\%$ complete data. We followed established modality-missing configurations and data processing protocols from recognized work [1, 44] to ensure methodological soundness.

Table 2: MIIAD Bench - Eyecandies Split with different missing types and rates.

Missing Rate	Type	3D PC in # Train	2D RGB in # Train	3D PC in # Test	2D RGB in # Test
30%	3D PC	7000	10000	2800	4000
	2D RGB	10000	7000	4000	2800
	Both	8500	8500	3400	3400
50%	3D PC	5000	10000	2000	4000
	2D RGB	10000	5000	4000	2000
	Both	7500	7500	3000	3000
70%	3D PC	3000	10000	1200	4000
	2D RGB	10000	3000	4000	1200
	Both	6500	6500	2600	2600

Evaluation Metrics. All evaluation metrics employed in our experiment align with those provided in the MVTec-3D AD [4] and Eyecandies [6] datasets. The image-level and pixel-level anomaly detection performance are evaluated with Area Under the Receiver Operating Curve (I-AUROC and P-AUROC, respectively), while the segmentation performance is assessed using Area Under the Per-Region Overlap (AUPRO).

4 RADAR

This section introduces the **Robust modAility-instructive fusing and Detecting frAmewoRk (RADAR)**. As shown in Fig. 2, the **RADAR** framework addresses the practical MIIAD challenges through two key components: **i) Stage1: Adaptive Instruction Fusion (Section 4.2)**: It employs modality-incomplete instructions with inserted learnable parameters to guide the multimodal Transformer in adapting to modality-incomplete scenarios, while utilizing HyperNetwork for adaptive learning. **ii) Stage2: Double-Pseudo Hybrid Detection (Section 4.3)**: It designs a Double-Pseudo Hybrid Module with a double-head structure to highlight the uniqueness of different modality combinations, and makes decisions based on MDM and OCSVM to mitigate overfitting issues.

4.1 Pre: 2D&3D Feature Extraction

If the modality data is incomplete, we use corresponding pseudo-inputs as substitutes: for 2D images, we employ a full-one pixel value image as the pseudo-input \tilde{x}^{m1} ; for 3D point clouds, we generate a full-one tensor as the pseudo-input \tilde{x}^{m2} with dimensions matching the read data size. When the modality data is complete, we extract features using the following approach.

2D Images Feature Extraction. We employ pretrained ViT [11] from HuggingFace [48] to extract 2D image features f_{rgb} , consistent with previous research. Due to space constraints, further details will not be provided.

3D Point Clouds Feature Extraction. The input point cloud \mathcal{P} is an unordered sequence of point positions in three-dimensional space, containing N_P points, which makes it challenging to extract meaningful features directly by feeding them into standard Transformer modules. We first divid the point cloud \mathcal{P} into M groups $\mathcal{P} = \{\mathcal{P}_1, \dots, \mathcal{P}_M\}$ using Farthest Point Sampling (FPS) [34]. For each group \mathcal{P}_i , we further extract feature vector \mathcal{T}_i utilizing a pretrained MaskTransformer [52] and Point-MAE [32], i.e., each group \mathcal{P}_i has a single point feature \mathcal{T}_i . We take the output of the Mask-Transformer as the initial point features $\mathcal{T}_{en} = [\mathcal{T}_{en1}, \dots, \mathcal{T}_{enM}]$. \mathcal{T}_{en}

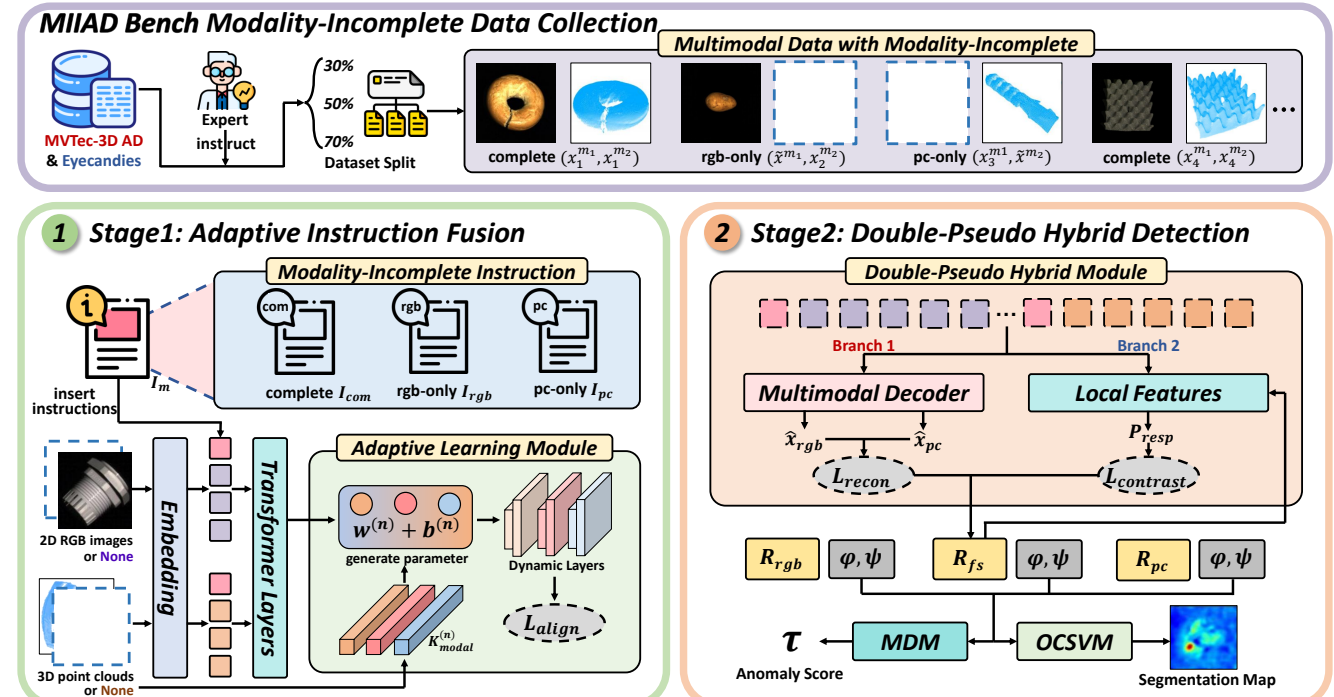


Figure 2: Overview of RADAR. It consists of three parts: i) **MIIAD Bench Data Collection**. Collecting data from the MVTec-3D AD dataset and constructing different data splits for the benchmark under the guidance of domain experts. ii) **Adaptive Instruction Fusion**. Prepending the modality-incomplete instruction I_m of multimodal data (x_i^{m1}, x_i^{m2}) into a simple multimodal Transformer input token, while introducing HyperNetwork to achieve adaptive parameter learning. iii) **Double-Pseudo Hybrid Detection**. Constructing a Double-Pseudo Hybrid Module for mitigating overfitting and feeding the features stored in multiple repositories R_{rgb} , R_{fs} , and R_{pc} into the MDM and OCSVM for anomaly score τ and segmentation map, respectively.

will be fed to Point-MAE to further improve the 3D point feature and take the decoder’s output as the extracted 3D point features $\mathcal{T} = [\mathcal{T}_1, \dots, \mathcal{T}_M]$, which can be denoted as $\mathcal{T} = \text{Decoder}_{MAE}(\mathcal{T}_{en})$.

After point interpolation and projection, we apply average pooling to derive 3D point cloud features f_{pc} .

4.2 Stage 1: Adaptive Instruction Fusion

For modality-incomplete scenarios, we maintain that focusing on existing modality features during fusion outweighs generating missing data. Inspired by prompt learning’s prefix-tuning [23], at Stage1, we construct modality-incomplete instructions (as learnable parameters) and insert them into the multimodal Transformer for feature fusion. And then propose an Adaptive Learning Module based on HyperNetWork for parameter optimization.

Modality-Incomplete Instruction. The distinct inputs between complete and incomplete modality data guide our learnable modality-incomplete instructions [23]. Thus, we create **modality-incomplete instructions** for each modality-incomplete scenario. These instructions are implemented as randomly initialized parameters.

As shown in Fig. 2, for IAD tasks involving two modalities, we configure $2^2 - 1 = 3$ different instructions, which are then prepended to the input tokens according to the modality-incomplete conditions. Only the instruction corresponding to a specific missing modality condition will be activated (i.e., trained). The input embedding feature of the j -th Multi-head Self-Attention (MSA) layer is represented as $h^j \in \mathbb{R}^{L_i \times d}$, $i = 1, 2, \dots, N$, where L_i is the instruction length and d is the embedding dimension. The function $F_{instruct}$

describing the instruction addition process can be expressed as:

$$F_{instruct}(i_m^j, h^j) = \text{concat}(i_m^j; h^j), \quad (1)$$

Instructed Feature Fusion. In RADAR, the multimodal Transformer simply prepends the modality-incomplete instruction i_m^j to the previously extracted 2D feature f_{rgb} and 3D feature f_{pc} at the j -th layer respectively. Thus, we form the modified embedding:

$$f_{ex_i}^j = F_{instruct}(f_m, h^j), \quad f_m \in \{f_{rgb}, f_{pc}\}, \quad (2)$$

The two new modified features can be represented as $\{\hat{f}_{pc}, \hat{f}_{rgb}\}$.

Subsequently, through Multi-Layer Perceptrons (MLPs) MLP_{pc} and MLP_{rgb} along with fully connected layers, the features of both modalities are mapped to $\{g_{pc}, g_{rgb}\}$. The final fusion learning uses patch-wise contrastive loss (InfoNCE Loss [42]) as the objective function, expressed as:

$$L_{align} = \frac{g_{pc} \cdot g_{rgb}^T}{\sum_{t=1}^{N_b} \sum_{k=1}^{N_p} g_{pc} \cdot g_{rgb}^T}, \quad (3)$$

where N_b is the batch size and N_p is the number of patches. The multimodal feature output from fully connected layer is called \hat{G} .

During training, the modality-incomplete instructions guide the model to learn features from the non-missing modality, enabling the model to better focus on the available effective feature information and achieve instructed feature fusion.

Adaptive Learning Module. Recent work [17] demonstrates HyperNetworks’ effectiveness for domain adaptation [29] tasks like modality-incomplete scenarios, as it can process data from different sources as a single source domain without requiring perfect feature alignment. Thus, we propose an Adaptive Learning Module to leverage HyperNetwork for adaptive parameter learning of learnable components (treated as “dynamic layers”) in Stage1.

Specifically, the HyperNetworks considers the parameters of the MLP layers as matrices $K^{(n)} \in \mathbb{R}^{N_{in} \times N_{out}}$, where N_{in} and N_{out} represent the number of input and output neurons in the n -th layer of the MLP, respectively. The creation process of $K^{(n)}$ can be viewed as matrix factorization, expressed as:

$$K^{(n)} = \xi(z^{(n)}; \Theta_p), \quad (4)$$

where both $z^{(n)}$ and $\xi(\cdot)$ are randomly initialized during training with parameters Θ_p . Different from conventional HyperNetworks, to adapt to different modality-missing conditions, we propose modeling the parameters by replacing $z^{(n)}$ with input features representing modality-missing conditions. Specifically, a layer-specific encoder $\xi^h(\cdot)$ encodes $\{\hat{f}_{pc}, \hat{f}_{rgb}\}$ into $e^{(n)}$. Then the HyperNetwork transforms $e^{(n)}$ into parameters, i.e., we input $e^{(n)}$ into the following two MLP layers to generate adaptive parameters:

$$w^{(n)} = (W_1 \xi^h(e^{(n)}) + B_1)W_2 + B_2, \quad (5)$$

where W_1 , W_2 , B_1 , and B_2 are the weights and bias terms of the first and second MLP layers. The model will adaptively adjust parameters based on different inputs, thereby enhancing robustness.

4.3 Stage2: Double-Pseudo Hybrid Detection

In stage2, since we used modality-incomplete instructions in stage1 to make the model focus more on existing modality features, this naturally leads to overfitting risks. For instance, when only 2D image data exists, the single-viewpoint 2D image may miss anomalies that would be visible in the absent 3D point cloud data. Requiring the model to predict anomalies using just 2D images could make it overfit to irrelevant features like lighting or textures [57].

To address this, we propose a Double-Pseudo Hybrid Module using pseudo-supervision to highlight modality-specific characteristics, followed by MDM and OCSVM-based anomaly detection using three feature repositories.

Double-Pseudo Hybrid Module. To mitigate overfitting, we employ two distinct supervisory signals in two branches to optimize the multimodal feature \hat{G} obtained from stage1, enabling it to learn diverse semantic information. Since MIAD is an unsupervised learning task, we construct two different pseudo-supervisions as follows:

For **Branch 1**, we impose global consistency constraints on \hat{G} through self-supervised reconstruction. Specifically, we introduce a multimodal decoder comprising a 2D RGB decoder and a 3D point cloud decoder. \hat{G} is fed into the decoder to obtain reconstructed RGB images \hat{x}_{rgb} and point clouds \hat{x}_{pc} , then we compute the reconstruction loss using Mean Square Error (MSE):

$$\mathcal{L}_{\text{recon}} = \lambda_{\text{rgb}} \cdot \text{MSE}(x_{\text{rgb}}, \hat{x}_{\text{rgb}}) + \lambda_{\text{pc}} \cdot \text{MSE}(x_{\text{pc}}, \hat{x}_{\text{pc}}) \quad (6)$$

where $\lambda_{\text{rgb}} = 1.0$ and $\lambda_{\text{pc}} = 0.5$ are weighting factors, and x_{rgb} and x_{pc} the original multimodal inputs. A detailed discussion of the weighting strategy is in Appendix Sec. 9.

For **Branch 2**, we provide local discriminative constraints for \hat{G} through contrastive learning. Specifically, we partition \hat{G} into local patches by spatial location and compress them via average pooling into feature vectors $\{g_1, g_2, \dots, g_M\}$ as local features. Simultaneously, we maintain a multimodal online feature bank R_{fs} , initially randomly initialized and gradually replaced with real features during training. For each local patch g_i , we compute cosine similarity with all features f_k^{Memory} in the bank and take the mean of top-K similarities as normality score s_i and pseudo anomaly score a_i :

$$s_i = \frac{1}{K} \sum_{k=1}^K \text{sim}(g_i, f_k^{\text{Memory}}) \quad (7)$$

$$a_i = 1 - s_i \quad (8)$$

Based on a_i , we get a low-resolution response map \mathbf{P}_{resp} by spatial reconstruction and obtain pseudo-labels y_p by thresholding:

$y_p = \begin{cases} 1, & \text{if } a_i > \sigma \\ 0, & \text{otherwise} \end{cases}$, where $\sigma = 0.35$ is a threshold. Finally, the contrastive loss is computed via Binary Cross-Entropy (BCE):

$$\mathcal{L}_{\text{contrast}} = \text{BCE}(\mathbf{P}_{\text{resp}}, y_p) \quad (9)$$

This double-branch design constrains model learn globally consistent features (avoiding sensitivity local noise) while focusing anomalous regions (preventing overfitting normal samples).

Repository-based Anomaly Detection. Subsequently, we use multiple repositories to store features. The 3D point cloud features, 2D RGB image features, and modality fusion features will be stored in repositories R_{pc} , R_{rgb} , and R_{fs} respectively. Each repository is capable of generating predicted anomaly scores and segmentation maps. Mahalanobis Distance Matrix (MDM) is used to predict the final anomaly score τ and OCSVM is used to predict the final segmentation map Seg_m :

$$\tau = \text{MDM}(\{\phi(R_{pc}, f_{pc}), \phi(R_{rgb}, f_{rgb}), \phi(R_{fs}, f_{fs})\}), \quad (10)$$

$$\text{Seg}_m = \text{OCSVM}(\{\psi(R_{pc}, f_{pc}), \psi(R_{rgb}, f_{rgb}), \psi(R_{fs}, f_{fs})\}), \quad (11)$$

where ϕ, ψ are the score functions introduced in PatchCore [36].

5 Experiments

5.1 Experimental Setup

Baselines. We conducted extensive comparative experiments with our RADAR model on **MIIAD Bench**: **i) MIAD methods:** Recent advanced MIAD approaches including Shape-Guided [8], M3DM [45], and the Multimodal Large Language Models (MLLM) based AnomalyGPT [14]. Following the methodology of [51], we also incorporated powerful MLLM models Gemini Vision Pro and GPT-4 Vision into comparisons using specific prompts. **ii) Missing-modality based methods:** Recent advanced missing-modality approaches including ShaSpec [44] using shared-specific feature modeling and CMDIAD [41] with cross-modal distillation strategy. Additional comparative methods are presented in Appendix Sec. 2.

Implementation Details. RADAR’s backbones consist of the following components: i) For 3D point cloud features, extraction is performed by MaskTransformer [52] and Point-MAE Decoder [32]. ii) For 2D RGB image features, the pre-trained ViTB/8 model with DINO is employed. Besides, we freeze all parameters of the multimodal Transformer backbone, focusing exclusively on training

Table 3: Performance comparison of different MIAD methods on *MIIAD Bench*. Red bold values indicate the best experimental performance, while underlined values denote the second-best results.

Missing Rate	MIIAD Bench Split	Data in # Train		Data in # Test		I-AUROC				AUPRO					
		3D PC	2D RGB	3D PC	2D RGB	GPT-4V	Anomaly-GPT [14]	M3DM [45]	Shape-Guided [8]	RADAR (Ours)	Gemini-V	GPT-4V	M3DM [45]	Shape-Guided [8]	RADAR (Ours)
0%	MVTec-3D AD	100%		100%		0.753	0.922	0.945	0.947	0.947	0.344	0.572	0.964	0.976	<u>0.967</u>
	Eye-candies	100%		100%		0.676	0.857	<u>0.897</u>	0.891	0.901	0.297	0.514	0.882	<u>0.876</u>	0.885
30%	MVTec-3D AD	100%	70%	100%	70%	0.682	0.841	0.892	0.910	<u>0.908</u>	0.315	0.544	0.911	<u>0.924</u>	0.925
		70%	100%	70%	100%	0.693	0.828	<u>0.883</u>	0.869	0.903	0.307	0.530	<u>0.932</u>	0.918	0.947
	Eye-candies	100%	70%	100%	70%	0.624	0.784	0.844	<u>0.864</u>	0.869	0.264	0.453	0.828	<u>0.832</u>	0.847
		70%	100%	70%	100%	0.615	0.788	<u>0.843</u>	0.837	0.858	0.248	0.458	<u>0.832</u>	0.829	0.851
50%	MVTec-3D AD	100%	50%	100%	50%	0.591	0.732	0.796	0.811	<u>0.810</u>	0.248	0.485	0.835	<u>0.848</u>	0.857
		50%	100%	50%	100%	0.584	0.724	<u>0.789</u>	0.773	0.821	0.261	0.489	<u>0.849</u>	0.838	0.874
	Eye-candies	75%	75%	75%	75%	0.587	0.718	0.791	<u>0.799</u>	0.817	0.253	0.483	<u>0.833</u>	0.831	0.862
		100%	50%	100%	50%	0.565	0.703	0.765	<u>0.786</u>	0.795	0.202	0.387	<u>0.749</u>	0.746	0.772
		50%	100%	50%	100%	0.559	0.695	<u>0.757</u>	0.756	0.780	0.206	0.375	<u>0.741</u>	0.741	0.769
70%	MVTec-3D AD	100%	30%	100%	30%	0.476	0.616	0.675	<u>0.685</u>	0.707	0.183	0.394	0.715	<u>0.729</u>	0.755
		30%	100%	30%	100%	0.488	0.608	<u>0.662</u>	0.649	0.703	0.184	0.401	<u>0.709</u>	0.696	0.748
	Eye-candies	65%	65%	65%	65%	0.484	0.615	0.668	<u>0.672</u>	0.706	0.178	0.398	0.711	<u>0.714</u>	0.752
		100%	30%	100%	30%	0.437	0.571	0.629	<u>0.635</u>	0.662	0.154	0.334	0.613	<u>0.616</u>	0.647
		30%	100%	30%	100%	0.429	0.565	<u>0.623</u>	0.611	0.654	0.162	0.328	<u>0.608</u>	0.602	0.649
		65%	65%	65%	65%	0.433	0.570	0.624	<u>0.626</u>	0.658	0.159	0.331	0.610	<u>0.615</u>	0.649

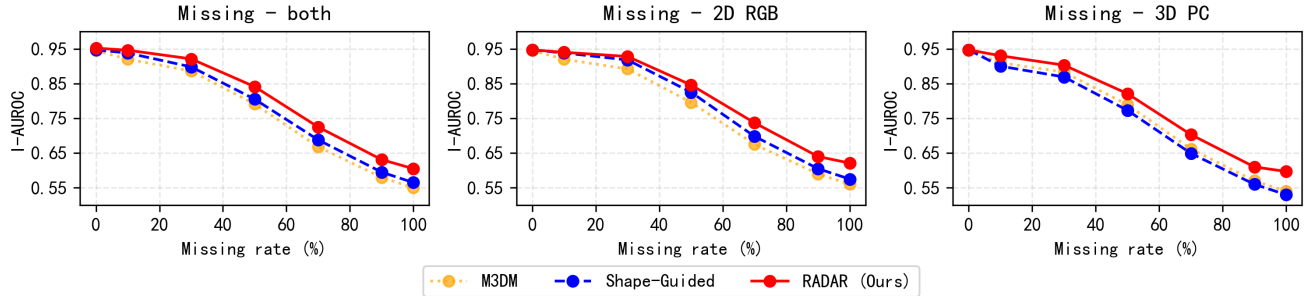


Figure 3: Quantitative results of I-AUROC on the *MIIAD Bench* - MVTEC-3D AD with different missing rates under different missing-modality scenarios. Each data point in the figure represents that training and testing are with the same $\eta\%$ missing rate.

parameters relevant to the downstream MIAD task. This approach significantly reduces computational costs during training. Further details of trainable components are provided in Appendix Sec. 1.

5.2 Results on *MIIAD Bench*

We compare **RADAR** with advanced MIAD models and missing-modality based methods on our ***MIIAD Bench***. Tab. 3 shows the experimental results of I-AUROC and AUPRO metrics between **RADAR** and other MIAD models on ***MIIAD Bench***, while P-AUROC results are presented in Appendix Sec. 5 and Sec. 7. Tab. 4 demonstrates comparisons between **RADAR** and missing-modality based methods. Take the performance of the model on ***MIIAD Bench*** - MVTEC-3D AD Split as an example, the results reveal:

i) We introduce a challenging and practical new task: Tab. 3 shows that the performance of advanced MIAD models degrades significantly with increasing modality missing rates. At 30% 3D point cloud missing rate, Shape-Guided [8] and M3DM [45] show I-AUROC drops of 6.2 points (6.5%) and 7.8 points (8.2%), and AUPRO drops of 3.2 points (3.3%) and 5.8 points (5.9%) respectively compared to complete modality. Performance declines dramatically

when missing rate exceeds 50%. For Shape-Guided [8], increasing 3D point cloud missing rate from 30% to 50% causes I-AUROC and AUPRO drops of 9.6 points (11.0%) and 8.0 points (8.7%); from 50% to 70%, drops increase to 12.4 points (16.0%) and 14.2 points (16.9%). This demonstrates the significant challenge posed by MIIAD, which is unavoidable in real-world applications. Tab. 4 shows existing missing-modality methods struggle with MIIAD. At 70% 3D point cloud missing rate, ShaSpec [44] and CMDIAD [41] only improve baseline I-AUROC by 0.9 points (1.3%) and -1.0 points (-1.5%), and AUPRO by 0.9 points (1.2%) and 0.3 points (0.4%). Qualitative results in Fig 3 confirm this trend across different missing modalities.

ii) Improving existing advanced MIAD methods: As Tab. 3 shows, our method excels in nearly all settings. Compared to M3DM baseline, we achieve I-AUROC improvements of 1.6 points (1.7%), 3.2 points (4.0%) and 4.1 points (6.2%) at 30%, 50% and 70% 3D point cloud missing rates respectively, with corresponding AUPRO gains of 1.5 points (3.9%), 2.5 points (2.9%) and 3.9 points (5.5%). Against Shape-Guided [8] (which outperforms M3DM with complete modality), we achieve I-AUROC advantages of 3.4 points (4.0%), 4.8 points (6.2%) and 5.4 points (8.3%), and AUPRO advantages of 2.9 points

Table 4: Performance comparison with methods aiming at addressing the modality-incomplete issue on *MIIAD Bench*.

Missing Rate	MIIAD Bench Split	Data in # Train		Data in # Test		I-AUROC				AUPRO			
		3D PC	2D RGB	3D PC	2D RGB	M3DM (Baseline) [45]	+Sha-Spec [44]	+CMDIAD [41]	+RADAR (Ours)	M3DM (Baseline) [45]	+Sha-Spec [44]	+CMDIAD [41]	+RADAR (Ours)
0%	MVTec-3D AD	100%		100%		0.945	0.943	0.948	0.947	0.964	0.958	0.960	0.967
	Eyecandies	100%		100%		0.897	0.891	0.898	0.901	0.882	0.882	0.884	0.885
30%	MVTec-3D AD	100%	70%	100%	70%	0.892	0.901	0.898	0.908	0.911	0.915	0.911	0.925
		70%	100%	70%	100%	0.883	0.887	0.894	0.903	0.932	0.938	0.916	0.947
		85%	85%	85%	85%	0.886	0.893	0.897	0.907	0.917	0.917	0.913	0.929
	Eye-candies	100%	70%	100%	70%	0.844	0.847	0.842	0.869	0.828	0.834	0.831	0.847
		70%	100%	70%	100%	0.843	0.851	0.845	0.858	0.832	0.841	0.838	0.851
		85%	85%	85%	85%	0.843	0.852	0.843	0.867	0.830	0.840	0.835	0.854
70%	MVTec-3D AD	100%	30%	100%	30%	0.675	0.679	0.654	0.707	0.715	0.717	0.703	0.755
		30%	100%	30%	100%	0.662	0.671	0.652	0.703	0.709	0.718	0.712	0.748
	Eye-candies	65%	65%	65%	65%	0.668	0.677	0.653	0.706	0.711	0.717	0.707	0.752
		100%	30%	100%	30%	0.629	0.634	0.615	0.662	0.613	0.614	0.606	0.647
		30%	100%	30%	100%	0.623	0.624	0.607	0.654	0.608	0.611	0.598	0.649
		65%	65%	65%	65%	0.624	0.626	0.610	0.658	0.610	0.613	0.601	0.649

Table 5: Ablation study of different modules under varying missing rates on *MIIAD Bench* - MVTec-3D AD. Here, MII, ALM, and DPHM represent Modality-Incomplete Instruction, Adaptive Learning Module, and Double-Pseudo Hybrid Module.

Methods	Setting			50% of pc		70% of pc	
	MII	ALM	DPHM	I-AUROC	AUPRO	I-AUROC	AUPRO
Baseline				0.789	0.849	0.662	0.709
+ MII	✓			0.802	0.860	0.680	0.725
+ ALM		✓		0.795	0.853	0.668	0.714
+ DPHM			✓	0.798	0.856	0.675	0.719
+ MII & ALM	✓	✓		0.810	0.865	0.688	0.732
+ MII & DPHM	✓		✓	0.816	0.868	0.693	0.738
+ ALM & DPHM		✓	✓	0.804	0.862	0.682	0.727
RADAR (Ours)	✓	✓	✓	0.821	0.874	0.703	0.748

(3.1%), 3.6 points (4.3%) and 5.2 points (7.4%) at respective missing rates. Fig 3 shows our consistent performance gains as missing rates increase. Notably, our model shows increasingly larger performance gains over the baseline and competing MIAD methods as missing rates escalate, evidencing our framework’s substantial improvements to current MIAD solutions.

iii) Outperforming missing-modality based methods: Tab. 4 demonstrates that using M3DM as the baseline, our approach shows stronger robustness over alternative modality-missing solutions. At 30% 3D point cloud missing rate, we surpass CMDIAD [41] and ShaSpec [44] by 0.9 points (1.0%) and 3.6 points (4.0%) in I-AUROC, and 3.1 points (3.4%) and 0.9 points (0.9%) in AUPRO. At 70% 3D point cloud missing rate, advantages increase to 5.1 points (7.8%) and 3.2 points (4.8%) in I-AUROC, and 3.6 points (5.0%) and 3.0 points (4.2%) in AUPRO. Notably, our model’s performance gains over the baseline and other missing-modality methods increase progressively with higher missing rates.

Similar patterns hold for 2D RGB missing case, both-modality missing case, and **MIIAD Bench** - Eyecandies Split. More additional comparative experiments are provided in Appendix Sec. 6.

5.3 Ablation Study

To evaluate effectiveness of each module in **RADAR**, we conducted comprehensive ablation studies on three key components: Modality-Incomplete Instruction (MII), Adaptive Learning Module (ALM), and Double-Pseudo Hybrid Module (DPHM). As shown in Tab. 5,

Table 6: Comparison with RGB-only and 3D-only methods on MVTec-3D AD. RADAR is trained with complete multimodal data but tested under 100% modality absence scenarios.

Methods	Data in # Test	I-AUROC	AUPRO	P-AUROC
RGB	PatchCore [36]		0.770	0.876
		100% 2D RGB	0.830	0.871
	CS-Flow [16]		0.858	0.943
	CMDIAD [41]			0.987
3D	M3DM [45]	0% 3D PC	0.850	0.942
			0.854	0.944
	FPFH [18]		0.782	0.924
	Shape-Guided [8]	100% 3D PC	0.916	0.931
	CMDIAD [41]		0.938	0.934
	M3DM [45]	0% 2D RGB	0.874	0.906
	RADAR (Ours)		0.907	0.932
				0.984

each module significantly improves baseline performance. At 50% 3D point cloud missing rate, these modules increase I-AUROC by 1.3 points (1.6%), 0.6 points (0.8%), and 0.9 points (1.1%), and AUPRO by 1.1 points (1.3%), 0.4 points (0.5%), and 0.7 points (0.8%) respectively. At 70% missing rate, modules improve I-AUROC by 1.8 points (2.7%), 0.6 points (0.9%), and 1.3 points (1.9%), and AUPRO by 1.6 points (2.3%), 0.5 points (0.7%), and 1.0 points (1.4%).

The results reveal that the MII contributes most to performance gains, proving its effect for modality-missing scenarios. The DPHM shows secondary importance, reflecting its overfitting mitigation. Finally, the role of ALM shows that dynamic parameter learning enhances performance. Similar experimental patterns are observed for other modality-missing cases, as presented in Appendix Sec. 8.

5.4 In-Depth Analysis

Comparisons with RGB-only, 3D-only methods. Although our **MIIAD Bench** does not follow a “Multi-modal Training, Few-modal Inference” setting, we rigorously conducted comparative experiments with RGB-only IAD models (using only 2D information) and 3D-only IAD models (relying solely on depth information), as shown in Tab. 6. In this comprehensive experiment, all models were trained on modality-complete data. When comparing with RGB-only models, the 2D RGB modality remains complete while the 3D point cloud data is entirely missing. Conversely, when evaluating against 3D-only models, the 3D point cloud modality stays

Table 7: Performance comparison of modality-incomplete in more situations.

Missing Rate	MIIAD Bench Split	Data in # Train		Data in # Test		I-AUROC				AUPRO					
		3D PC	2D RGB	3D PC	2D RGB	GPT-4V	Anomaly-GPT [14]	M3DM [45]	Shape-Guided [8]	RADAR (Ours)	Gemini-V	GPT-4V	M3DM [45]	Shape-Guided [8]	RADAR (Ours)
0%	MVTec-3D AD	100%		100%		0.753	0.922	0.945	0.947	0.947	0.342	0.574	0.964	0.976	0.967
	Eye-candies	100%		100%		0.676	0.857	<u>0.897</u>	0.891	0.901	0.297	0.514	<u>0.882</u>	0.876	0.885
30%	MVTec-3D AD	100%		85%		0.714	0.876	0.891	<u>0.897</u>	0.915	0.320	0.543	0.924	<u>0.928</u>	0.934
	Eye-candies	85%		85%		0.706	0.858	<u>0.871</u>	0.870	0.895	0.307	0.537	0.904	<u>0.916</u>	0.920
70%	MVTec-3D AD	100%		65%		0.651	0.816	0.849	<u>0.861</u>	0.877	0.268	0.477	0.844	<u>0.852</u>	0.868
	Eye-candies	65%		100%		0.639	0.814	0.831	<u>0.837</u>	0.848	0.251	0.463	0.814	<u>0.819</u>	0.843

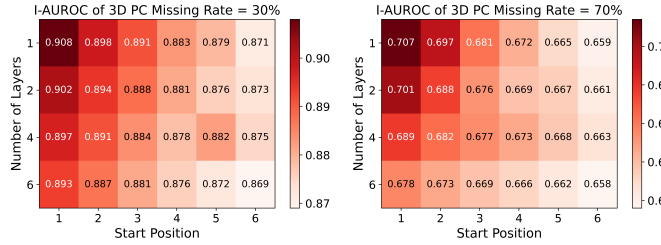


Figure 4: Effect of the position of instruction layers.

complete with completely missing 2D RGB data. This presents a significant challenge for **RADAR**, yet the table shows our model achieves the best AUPRO (0.944) and P-AUROC (0.989) in RGB-only scenarios. In 3D-only conditions, our model ranks second only to the specialized CMDIAD [41] model designed for this setting, achieving optimal P-AUROC (0.984) and suboptimal AUPRO (0.932). These results demonstrate our model’s capability to handle extreme cases of complete modality absence.

Robustness of modality-incomplete in more situations. In **MIIAD Bench**, the modality missing conditions during training and testing are identical, so we further investigated scenarios where these conditions differ. As shown in Tab. 7, for a 30% modality missing rate, this means both 2D RGB and 3D point cloud modalities have 15% missing during either training or testing (totaling 30%), while the corresponding training or testing data remains modality-complete. The same applies to the 70% missing rate. The table shows our model still outperforms other MIAD models. Taking MVTec-3D AD Split as an example, when test data has 30% modality missing rate, our model improves I-AUROC and AUPRO by 2.4 points (2.7%) and 1.0 points (1.1%) respectively compared to the M3DM. With 30% missing rate in training data, these improvements become 2.4 points (2.8%) and 1.6 points (1.8%). Similar performance is observed at 70% missing rate, further demonstrating our model’s robustness.

Computational costs. We reduce computational costs by freezing the multimodal Transformer parameters and only training downstream task-related parameters. Experiments show this reduces parameters by 98.66% versus the baseline. Our parameter efficiency reflects the real-time capability of our approach for practical MIIAD tasks. See Appendix Sec. 3 for details. It also explains why current MLLMs struggle with MIIAD tasks: they cannot effectively process 3D point clouds and suffer from excessive computational costs.

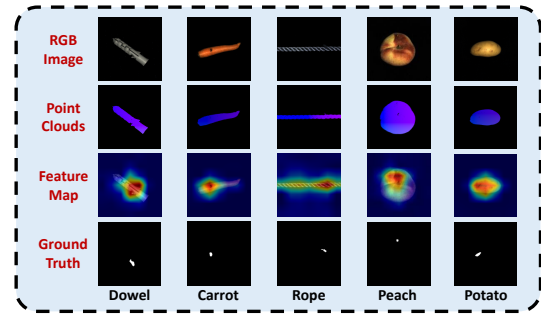


Figure 5: Visualization results of IAD.

Effect of the position of instruction layers. To thoroughly analyze the effectiveness of modality-incomplete instruction insertion positions, we visualize the effects of inserting instructions at different Transformer layers under various modality-missing scenarios, as shown in Fig. 4. The results demonstrate that the choice of instruction layers significantly impacts model performance. Inserting modality-incomplete instructions at earlier layers with fewer inserted layers yields better results. This likely occurs because earlier-layer features retain more modality-specific characteristics compared to deeper layers. With instructions, multimodal inputs begin fusion from the very first Transformer layer, with fusion intensity increasing at deeper layers. Consequently, modality-incomplete instructions prove more effective when applied to earlier layers. Recent studies [23] have provided similar insights.

Visualization results of IAD. Fig. 5 illustrates IAD visualization results of our model. It showcases our model’s aptitude for accurately identifying anomalies across diverse categories.

6 Conclusion

We propose the first-kind-of work to comprehensively investigate the **Modality-Incomplete Industrial Anomaly Detection (MIIAD)** with corresponding benchmark **MIIAD Bench**, and construct a corresponding novel **Robust modAlity-instructive fusing and Detecting frAmewoRk**, abbreviated as **RADAR**. Extensive experiments indicated that our model outperforms other methods on **MIIAD Bench**. We believe that the proposed MIIAD task and **RADAR** serve as a complement to existing literature and provide new insights to the industrial anomaly detection community.

7 Acknowledgment

This work has been supported in part by the NSFC (No. 62402426, 62272411, 62441617), the Key Research and Development Projects in Zhejiang Province (No. 2025C01128, 2024C01106, 2025C01030, 2025C02156), Ningbo Yongjiang Talent Introduction Programme (2023A-400-G), Fundamental Research Funds for the Central Universities (226-2025-00057), Zhejiang University Education Foundation Qizhen Scholar Foundation.

References

- [1] Hangbo Bao, Wenhui Wang, Li Dong, Qiang Liu, Owais Khan Mohammed, Kriti Aggarwal, Subhajit Som, Songhao Piao, and Furu Wei. 2022. VLMo: Unified Vision-Language Pre-Training with Mixture-of-Modality-Experts. In *Advances in Neural Information Processing Systems*. <https://openreview.net/forum?id=bydKs84JEyw>
- [2] Paul Bergmann, Kilian Batzner, Michael Fauser, David Sattlegger, and Carsten Steger. 2022. Beyond dents and scratches: Logical constraints in unsupervised anomaly detection and localization. *International Journal of Computer Vision* 130, 4 (2022), 947–969.
- [3] Paul Bergmann, Michael Fauser, David Sattlegger, and Carsten Steger. 2020. Uninformed students: Student-teacher anomaly detection with discriminative latent embeddings. In *Proceedings of the IEEE/CVF conference on computer vision and pattern recognition*. 4183–4192.
- [4] Paul Bergmann, Xin Jin, David Sattlegger, and Carsten Steger. 2022. The MVTEC 3D-AD Dataset for Unsupervised 3D Anomaly Detection and Localization. In *Proceedings of the 17th International Joint Conference on Computer Vision*. 202–213.
- [5] Paul Bergmann and David Sattlegger. 2023. Anomaly detection in 3d point clouds using deep geometric descriptors. In *Proceedings of the IEEE/CVF Winter Conference on Applications of Computer Vision*. 2613–2623.
- [6] Luca Bonfiglioli, Marco Toschi, Davide Silvestri, Nicola Fioraiò, and Daniele De Gregorio. 2022. The EyeCandies Dataset for Unsupervised Multimodal Anomaly Detection and Localization. In *Proceedings of the Asian Conference on Computer Vision (ACCV)*. 3586–3602.
- [7] Cheng Chen, Qi Dou, Yueming Jin, Hao Chen, Jing Qin, and Pheng-Ann Heng. 2019. Robust multimodal brain tumor segmentation via feature disentanglement and gated fusion. In *Medical Image Computing and Computer Assisted Intervention-MICCAI 2019: 22nd International Conference, Shenzhen, China, October 13–17, 2019, Proceedings, Part III* 22. Springer, 447–456.
- [8] Yu-Min Chu, Chiel Liu, Ting-I Hsieh, Hwann-Tzong Chen, and Tyng-Luh Liu. 2023. Shape-Guided Dual-Memory Learning for 3D Anomaly Detection. In *Proceedings of the 40th International Conference on Machine Learning*. 6185–6194.
- [9] David Dehaene and Pierre Eline. 2020. Anomaly localization by modeling perceptual features. *arXiv preprint arXiv:2008.05369* (2020).
- [10] Jia Deng, Wei Dong, Richard Socher, Li-Jia Li, Kai Li, and Li Fei-Fei. 2009. Imagenet: A large-scale hierarchical image database. In *IEEE Conference on Computer Vision and Pattern Recognition (CVPR)*. 248–255.
- [11] Alexey Dosovitskiy, Lucas Beyer, Alexander Kolesnikov, Dirk Weissenborn, Xiaohua Zhai, Thomas Unterthiner, Mostafa Dehghani, Matthias Minderer, Georg Heigold, Sylvain Gelly, Jakob Uszkoreit, and Neil Houlsby. 2021. An Image is Worth 16x16 Words: Transformers for Image Recognition at Scale. In *Proceedings of the 9th International Conference on Learning Representations, ICLR 2021*. 3–7.
- [12] Martin A Fischler and Robert C Bolles. 1981. Random sample consensus: a paradigm for model fitting with applications to image analysis and automated cartography. *Commun. ACM* 24, 6 (1981), 381–395.
- [13] Minghe Gao, Xuqi Liu, Zhongqi Yue, Yang Wu, Shuang Chen, Juncheng Li, Siliang Tang, Fei Wu, Tat-Seng Chua, and Yueting Zhuang. 2025. Benchmarking Multimodal CoT Reward Model Stepwise by Visual Program. *arXiv:2504.06606* [cs.CV] <https://arxiv.org/abs/2504.06606>
- [14] Zhaopeng Gu, Bingke Zhu, Guibo Zhu, Yingying Chen, Ming Tang, and Jinqiao Wang. 2023. AnomalyGPT: Detecting Industrial Anomalies using Large Vision-Language Models. *arXiv preprint arXiv:2308.15366* (2023).
- [15] Denis Gudovskiy, Shun Ishizaka, and Kazuki Kozuka. 2022. CFLOW-AD: Real-Time Unsupervised Anomaly Detection with Localization via Conditional Normalizing Flows. In *2022 IEEE/CVF Winter Conference on Applications of Computer Vision (WACV)*. 1819–1828. doi:10.1109/WACV51458.2022.00188
- [16] Denis Gudovskiy, Shun Ishizaka, and Kazuki Kozuka. 2022. CFLOW-AD: Real-Time Unsupervised Anomaly Detection With Localization via Conditional Normalizing Flows. In *Proceedings of the IEEE/CVF Winter Conference on Applications of Computer Vision (WACV)*. 98–107.
- [17] David Ha, Andrew M. Dai, and Quoc V. Le. 2017. HyperNetworks. In *5th International Conference on Learning Representations, ICLR 2017*.
- [18] Eliahu Horwitz and Yedid Hoshen. 2022. An Empirical Investigation of 3D Anomaly Detection and Segmentation. *arXiv preprint arXiv:2203.05550* (2022).
- [19] Eliahu Horwitz and Yedid Hoshen. 2023. Back to the feature: classical 3d features are (almost) all you need for 3d anomaly detection. In *Proceedings of the IEEE/CVF Conference on Computer Vision and Pattern Recognition*. 2967–2976.
- [20] Chuanfei Hu, Kai Chen, and Hang Shao. 2021. A semantic-enhanced method based on deep SVDD for pixel-wise anomaly detection. In *2021 IEEE International Conference on Multimedia and Expo (ICME)*. IEEE, 1–6.
- [21] Jielin Jiang, Jiah Zhu, Muhammad Bilal, Yan Cui, Neeraj Kumar, Ruihan Dou, Feng Su, and Xiaolong Xu. 2022. Masked swin transformer unet for industrial anomaly detection. *IEEE Transactions on Industrial Informatics* 19, 2 (2022), 2200–2209.
- [22] Rabeeh Karimi Mahabadi, Sebastian Ruder, Mostafa Dehghani, and James Henderson. 2021. Parameter-efficient Multi-task Fine-tuning for Transformers via Shared Hypernetworks. In *Proceedings of the 59th Annual Meeting of the Association for Computational Linguistics and the 11th International Joint Conference on Natural Language Processing (Volume 1: Long Papers)*. Chengqing Zong, Fei Xia, Wenjie Li, and Roberto Navigli (Eds.). Association for Computational Linguistics, Online, 565–576. doi:10.18653/v1/2021.acl-long.47
- [23] Yi-Lun Lee, Yi-Hsuan Tsai, Wei-Chen Chiu, and Chen-Yu Lee. 2023. Multimodal Prompting with Missing Modalities for Visual Recognition. In *IEEE Conference on Computer Vision and Pattern Recognition (CVPR)*.
- [24] Juncheng Li, Xin He, Longhui Wei, Long Qian, Linchao Zhu, Lingxi Xie, Yueting Zhuang, Qi Tian, and Siliang Tang. 2022. Fine-grained semantically aligned vision-language pre-training. *Advances in neural information processing systems* 35 (2022), 7290–7303.
- [25] Juncheng Li, Kaihang Pan, Zhiqi Ge, Minghe Gao, Wei Ji, Wenqiao Zhang, Tat-Seng Chua, Siliang Tang, Hanwang Zhang, and Yueting Zhuang. 2023. Fine-tuning multimodal llms to follow zero-shot demonstrative instructions. In *The Twelfth International Conference on Learning Representations*.
- [26] Juncheng Li, Siliang Tang, Linchao Zhu, Wenqiao Zhang, Yi Yang, Tat-Seng Chua, Fei Wu, and Yueting Zhuang. 2023. Variational Cross-Graph Reasoning and Adaptive Structured Semantics Learning for Compositional Temporal Grounding. *IEEE Transactions on Pattern Analysis and Machine Intelligence* 45, 10 (2023), 12601–12617. doi:10.1109/TPAMI.2023.3274139
- [27] Yufei Liang, Jiangning Zhang, Shiwei Zhao, Runze Wu, Yong Liu, and Shuwen Pan. 2023. Omni-frequency channel-selection representations for unsupervised anomaly detection. *IEEE Transactions on Image Processing* (2023).
- [28] Tianwei Lin, Wenqiao Zhang, Sijing Li, Yuqian Yuan, Binhe Yu, Haoyuan Li, Wanggui He, Hao Jiang, Mengze Li, Xiaohui Song, et al. 2025. HealthGPT: A Medical Large Vision-Language Model for Unifying Comprehension and Generation via Heterogeneous Knowledge Adaptation. *arXiv preprint arXiv:2502.09838* (2025).
- [29] Jiang Liu, Bolin Li, Haoyuan Li, Tianwei Lin, Wenqiao Zhang, Tao Zhong, Zhenlin Yu, Jinghao Wei, Hao Cheng, Wanggui He, Fangxun Shu, Hao Jiang, Zheqi Lv, Juncheng Li, Siliang Tang, and Yueting Zhuang. 2025. Boosting Private Domain Understanding of Efficient MLLMs: A Tuning-free, Adaptive, Universal Prompt Optimization Framework. *arXiv:2412.19684* [cs.AI] <https://arxiv.org/abs/2412.19684>
- [30] Mengmeng Ma, Jian Ren, Long Zhao, Davide Testuggine, and Xi Peng. 2022. Are multimodal transformers robust to missing modality? In *Proceedings of the IEEE/CVF Conference on Computer Vision and Pattern Recognition*. 18177–18186.
- [31] Mengmeng Ma, Jian Ren, Long Zhao, Sergey Tulyakov, Cathy Wu, and Xi Peng. 2021. Smil: Multimodal learning with severely missing modality. In *Proceedings of the AAAI Conference on Artificial Intelligence*, Vol. 35. 2302–2310.
- [32] Yatian Pang, Wenxiao Wang, Francis EH Tay, Wei Liu, Yonghong Tian, and Li Yuan. 2022. Masked autoencoders for point cloud self-supervised learning. In *Computer Vision–ECCV 2022: 17th European Conference, Tel Aviv, Israel, October 23–27, 2022, Proceedings, Part II*. Springer, 604–621.
- [33] Petra Poklukar, Miguel Vasco, Hang Yin, Francisco S Melo, Ana Paiva, and Danica Kragic. 2022. Geometric Multimodal Contrastive Representation Learning. *arXiv preprint arXiv:2202.03390* (2022).
- [34] Charles Ruizhongtai Qi, Li Yi, Hao Su, and Leonidas J Guibas. 2017. PointNet++: Deep Hierarchical Feature Learning on Point Sets in a Metric Space. In *Advances in Neural Information Processing Systems*, I. Guyon, U. Von Luxburg, S. Bengio, H. Wallach, R. Fergus, S. Vishwanathan, and R. Garnett (Eds.), Vol. 30. Curran Associates, Inc. https://proceedings.neurips.cc/paper_files/paper/2017/file/d8bf84be3800d12f74d8b05e9b89836f-Paper.pdf
- [35] Tianyi Qin, Bo Peng, Jianjun Lei, Yuxuan Yao, and Qingming Huang. 2025. Modeling Intra- and Inter-Modal Correlations for Incomplete Multi-Modal 3D Shape Clustering. *IEEE Transactions on Multimedia* 27 (2025), 3833–3843. doi:10.1109/TMM.2025.3535317
- [36] Karsten Roth, Laitha Pemula, Joaquin Zepeda, Bernhard Schölkopf, Thomas Brox, and Peter Gehler. 2022. Towards Total Recall in Industrial Anomaly Detection. In *Proceedings of the IEEE/CVF Conference on Computer Vision and Pattern Recognition (CVPR)*. 14318–14328.
- [37] Karsten Roth, Laitha Pemula, Joaquin Zepeda, Bernhard Schölkopf, Thomas Brox, and Peter Gehler. 2022. Towards Total Recall in Industrial Anomaly Detection. In *IEEE Conference on Computer Vision and Pattern Recognition (CVPR)*. 14318–14328.
- [38] Marco Rudolph, Tom Wehrbein, Bodo Rosenhahn, and Bastian Wandt. 2023. Asymmetric Student-Teacher Networks for Industrial Anomaly Detection. In *Proceedings of the IEEE/CVF Winter Conference on Applications of Computer Vision (WACV)*. 2592–2602.

[39] Mohammadreza Salehi, Niousha Sadjadi, Soroosh Baselizadeh, Mohammad H Rohban, and Hamid R Rabiee. 2021. Multiresolution knowledge distillation for anomaly detection. In *Proceedings of the IEEE/CVF conference on computer vision and pattern recognition*. 14902–14912.

[40] Jouwon Song, Kyeongbo Kong, Ye-In Park, Seong-Gyun Kim, and Suk-Ju Kang. 2021. AnoSeg: Anomaly segmentation network using self-supervised learning. *arXiv preprint arXiv:2110.03396* (2021).

[41] Wenbo Sui, Daniel Lichau, Josselin Lefèvre, and Harold Phelipeau. 2024. Incomplete Multimodal Industrial Anomaly Detection via Cross-Modal Distillation. *arXiv:2405.13571 [cs.CV]* <https://arxiv.org/abs/2405.13571>

[42] Aäron van den Oord, Yazhe Li, and Oriol Vinyals. 2018. Representation Learning with Contrastive Predictive Coding. *ArXiv abs/1807.03748* (2018). <https://api.semanticscholar.org/CorpusID:49670925>

[43] Gijs van Tulder and Marleen de Bruijne. 2018. Learning cross-modality representations from multi-modal images. *IEEE transactions on medical imaging* 38, 2 (2018), 638–648.

[44] Hu Wang, Yuanhong Chen, Congbo Ma, Jodie Avery, Louise Hull, and Gustavo Carneiro. 2023. Multi-modal learning with missing modality via shared-specific feature modelling. In *Proceedings of the IEEE/CVF Conference on Computer Vision and Pattern Recognition*. 15878–15887.

[45] Yue Wang, Jinlong Peng, Jiangning Zhang, Ran Yi, Yabiao Wang, and Chengjie Wang. 2023. Multimodal industrial anomaly detection via hybrid fusion. In *Proceedings of the IEEE/CVF Conference on Computer Vision and Pattern Recognition*. 8032–8041.

[46] Shun Wei, Jielin Jiang, and Xiaolong Xu. 2025. UniNet: A Contrastive Learning-guided Unified Framework with Feature Selection for Anomaly Detection. (2025).

[47] Shicai Wei, Chunbo Luo, and Yang Luo. 2023. MMA-Net: Margin-Aware Distillation and Modality-Aware Regularization for Incomplete Multimodal Learning. In *Proceedings of the IEEE/CVF Conference on Computer Vision and Pattern Recognition (CVPR)*. 20039–20049.

[48] Thomas Wolf, Lysandre Debut, Victor Sanh, Julien Chaumond, Clement Delangue, Anthony Moi, Pierric Cistac, Tim Rault, Rémi Louf, Morgan Funtowicz, Joe Davison, Sam Shleifer, Patrick von Platen, Clara Ma, Yacine Jernite, Julien Plu, Canwen Xu, Teven Le Scao, Sylvain Gugger, Mariama Drame, Quentin Lhoest, and Alexander M. Rush. 2020. Transformers: State-of-the-Art Natural Language Processing. In *Proceedings of the 2020 Conference on Empirical Methods in Natural Language Processing: System Demonstrations*. Association for Computational Linguistics, Online, 38–45. <https://www.aclweb.org/anthology/2020.emnlp-demos.6>

[49] Julian Wyatt, Adam Leach, Sebastian M Schmon, and Chris G Willcocks. 2022. Anoddpm: Anomaly detection with denoising diffusion probabilistic models using simplex noise. In *Proceedings of the IEEE/CVF Conference on Computer Vision and Pattern Recognition*. 650–656.

[50] Jiacong Xu, Shao-Yuan Lo, Bardia Safaei, Vishal M. Patel, and Isht Dwivedi. 2025. Towards Zero-Shot Anomaly Detection and Reasoning with Multimodal Large Language Models. *arXiv:2502.07601 [cs.CV]* <https://arxiv.org/abs/2502.07601>

[51] Xiaohao Xu, Yunkang Cao, Yongqi Chen, Weiming Shen, and Xiaonan Huang. 2024. Customizing Visual-Language Foundation Models for Multi-modal Anomaly Detection and Reasoning. *arXiv preprint arXiv:2403.11083* (2024).

[52] Xumin Yu, Lulu Tang, Yongming Rao, Tiejun Huang, Jie Zhou, and Jiwen Lu. 2022. Point-BERT: Pre-Training 3D Point Cloud Transformers with Masked Point Modeling. In *Proceedings of the IEEE Conference on Computer Vision and Pattern Recognition (CVPR)*.

[53] Yuqian Yuan, Hang Zhang, Wentong Li, Zesen Cheng, Boqiang Zhang, Long Li, Xin Li, Deli Zhao, Wenqiao Zhang, Yuetong Zhuang, et al. 2024. Videorefer suite: Advancing spatial-temporal object understanding with video llm. *arXiv preprint arXiv:2501.00599* (2024).

[54] Chaohe Zhang, Xu Chu, Liantao Ma, Yinghao Zhu, Yasha Wang, Jiangtao Wang, and Junfeng Zhao. 2022. M3Care: Learning with Missing Modalities in Multimodal Healthcare Data. In *Proceedings of the 28th ACM SIGKDD Conference on Knowledge Discovery and Data Mining (KDD '22)*. ACM, 2418–2428. doi:10.1145/3534678.3539388

[55] Wenqiao Zhang, Tianwei Lin, Jiang Liu, Fangxun Shu, Haoyuan Li, Lei Zhang, He Wanggui, Hao Zhou, Zheqi Lv, Hao Jiang, et al. 2024. Hyperllava: Dynamic visual and language expert tuning for multimodal large language models. *arXiv preprint arXiv:2403.13447* (2024).

[56] Wenqiao Zhang, Lei Zhu, James Hallinan, Shengyu Zhang, Andrew Makmur, Qingpeng Cai, and Beng Chin Ooi. 2022. Boostmrs: Boosting medical image semi-supervised learning with adaptive pseudo labeling and informative active annotation. In *Proceedings of the IEEE/CVF Conference on Computer Vision and Pattern Recognition*. 20666–20676.

[57] Yunhua Zhang, Hazel Doughty, and Cees Snoek. 2023. Learning Unseen Modality Interaction. In *Advances in Neural Information Processing Systems*, A. Oh, T. Nau mann, A. Globerson, K. Saenko, M. Hardt, and S. Levine (Eds.), Vol. 36. Curran Associates, Inc., 54716–54726. https://proceedings.neurips.cc/paper_files/paper/2023/file/abb4847bb60f38b1b7649d26c7a0067-Paper-Conference.pdf

[58] Zheng Zhang and Xiaogang Deng. 2021. Anomaly detection using improved deep SVDD model with data structure preservation. *Pattern Recognition Letters*

Appendix

This is the Appendix for the paper “Robust Modality-Incomplete Anomaly Detection: a Modality-Instructive Framework with Benchmark”, which provides supplementary materials, detailed proofs, and additional experimental results to support the findings presented in the main manuscript. Tab. 8 shows abbreviations and symbols used in the main paper.

Table 8: Abbreviations and symbols used in the main paper.

Abbreviation / Symbol	Meaning
<i>Abbreviation</i>	
RADAR	Robust modAlity-instructive fusing and Detecting frAmewoRk
MIAD	Modality-Incomplete Industrial Anomaly Detection
AIF	Adaptive Instruction Fusion
MII	Modality-Incomplete Instruction
ALM	Adaptive Learning Module
DPHM	Double-Pseudo Hybrid Module
MLP	Multi-Layer Perceptron
<i>Symbol in Algorithm</i>	
\mathcal{D}^C	Modality-Complete Subset Data
$\tilde{\mathcal{D}}^{2D}$	3D Point Cloud Modality-Incomplete Subset Data
$\tilde{\mathcal{D}}^{3D}$	2D RGB Image Modality-Incomplete Subset Data
I_m	Modality-Incomplete Instructions
I_{pc}	MII for 3D Point Cloud Modality-Missing
I_{rgb}	MII for 2D RGB Image Modality-Missing
f_{pc}	Features of 3D Point Clouds
f_{rgb}	Features of 2D RGB Images
BCE	Binary Cross-Entropy
$OCSVM$	One-Class Support Vector Machine
MDM	Mahalanobis Distance Matrix

In this supplementary material we present:

- Section A provides detailed information on the **RADAR** model construction and training processes not covered in the main paper.
- Section B provides a detailed description of the experimental settings in the main paper, including comparisons with both MIAD methods and missing-modality based approaches.
- Section C analyzes the parameter efficiency of **RADAR**, demonstrating that the framework requires minimal computational overhead.
- Section D provides the algorithmic pseudocode for **RADAR**, abstracting the pipeline workflow of the framework.
- Section E presents expanded comparative experiments between **RADAR** and MIAD methods.
- Section F provides additional comparisons of **RADAR** with missing-modality based approaches.
- Section G supplements qualitative experiments for P-AUROC and AUPRO metrics.
- Section H elivers more comprehensive ablation studies.
- Section J conducts systematic in-depth analysis of hyperparameter ablation studies and selection.
- Section K offers extended visualization results for industrial anomaly detection.

A Implementation Details

The backbone network of **RADAR** consists of the following pre-trained components: **i) For 3D point clouds**, we adopt a combination of MaskTransformer [52] and Point-MAE Decoder [32] architectures to extract features. MaskTransformer uses transformer-based masked point modeling to capture long-range contextual relationships, while Point-MAE employs a masked autoencoding paradigm that effectively learns geometric representations from incomplete point clouds, making them particularly effective for 3D feature extraction. **ii) For 2D RGB images**, we use a Vision Transformer (ViT), specifically the ViT-B/8 model pre-trained on ImageNet [10] with DINO framework that demonstrates strong anomaly detection capabilities. Both 2D&3D feature extraction backbones are pre-trained models with powerful feature extraction capabilities, requiring no additional retraining.

During data loading, when modalities are incomplete: **i) For missing 3D point cloud data** (encapsulated in TIFF format), we generate a pseudo-input \tilde{x}^{m_1} as a tensor filled with ones matching original data dimensions. **ii) For missing 2D RGB image data**, we create a pseudo-image \tilde{x}^{m_2} with all pixel values set to 1. We use RANSAC [12] to estimate background planes in 3D point clouds, removing points within 0.005 distance threshold. Following M3DM [45], we resize both positional tensors and 2D images to 224×224 , and convert outputs from layers $\{3, 7, 11\}$ into x, y, z coordinates to represent 3D features.

During training, we freeze all parameters of the multimodal Transformer backbone and only train downstream task MIAD-related parameters. Learnable components in **RADAR** include: modality-incomplete instruction, HyperNetwork (implemented as 2-layer MLP), MLPs (MLP_{rgb} and MLP_{pc}) in Stage1-Instructed Feature Fusion, multimodal decoders in DPHM Branch 1 (2D decoder with 3 transposed conv layers; 3D decoder with MLP), upsampling network in DPHM Branch 1, and OCSVM in Stage2. Most components are lightweight (e.g., implemented with 1 – 2 MLP layers). Below, we will discuss the implementation details of several main learnable modules: **i) Modality-Incomplete Instruction**, with a default length L_i set to 16. The MSA layer index with the prepended instruction ranges from 0 to 3. The optimizer utilized is AdamW, with the learning rate set to 1×10^{-2} . **ii) MLP_{rgb} and MLP_{pc}** : use AdamW as the optimizer, a learning rate of 1×10^{-3} , and a batch size of 16. **iii) OCSVM**: is optimized using SGD, with a learning rate of 1×10^{-4} . Further details are available in the appendix.

The threshold σ for generating pseudo-labels y_p in the DPHM Branch 1 is set as 0.35. we directly took 30% of the data samples and analyzed the anomaly score distribution of normal samples. We obtained all anomaly scores a_i , then took the 95% as our reference threshold σ (where 95% of normal samples’ a_i are below this value), ultimately obtaining a value of 0.35.

B Experimental Setting

Beyond the comparisons with MIAD methods and missing-modality based methods discussed in the main text, our **RADAR** model has been extensively evaluated against additional relevant approaches.

B.1 MIAD Methods

To demonstrate how our **RADAR** model improves existing advanced MIAD methods, we conducted comprehensive comparative experiments on **MIAD Bench** with Shape-Guided [8], M3DM [45], AST [38], BTF [19], AnomalyGPT [14] which is based on MLLM [13, 24–26, 28, 53, 55, 56], Gemini Vision Pro (using specific prompts), and GPT-4 Vision (using specific prompts). Below we briefly introduce these models (excluding Gemini Vision Pro and GPT-4 Vision):

Shape-Guided [8]: Integrates color and geometric modalities using two specialized expert models and dual memory banks to achieve state-of-the-art performance in 3D anomaly detection.

M3DM [45]: Proposes a multimodal industrial anomaly detection method with hybrid fusion, utilizing unsupervised feature fusion and decision layer fusion to enhance detection and segmentation performance on 3D point clouds and RGB images.

AST [38]: Proposes asymmetric student-teacher networks for anomaly detection, using a bijective normalizing flow as the teacher and a conventional feed-forward network as the student to enhance anomaly detection performance.

BTF [19]: Proposes a method that combines classical 3D features (FPFH) with color-based features (PatchCore) to achieve state-of-the-art performance in 3D anomaly detection, emphasizing the importance of rotation invariance and complementary benefits of 3D and color modalities.

AnomalyGPT [14]: Leverages large vision-language models (LVLMs) to detect and localize industrial anomalies by fine-tuning on simulated anomaly data and employing a lightweight decoder for pixel-level localization, eliminating the need for manual threshold adjustments.

While general foundation models like **Gemini Vision Pro** and **GPT-4 Vision** possess broad knowledge, their inability to process 3D point clouds and the contextual differences across industrial anomalies limit their effectiveness for diverse industrial inspection needs. Following [51], we convert 3D point clouds into depth maps through planar projection, transforming them into standard 2D image formats readable by foundation models. We then design specific prompts including: *Task instruction* (Clear task information prompts the generic foundation model for effective anomaly detection), *Class context* (Explicit class context information, represented by a class token [CLS], enhances the model’s recognition of the target domain), and *Normality criteria* (Language-form rules define explicit normal standards and describe abnormal objects and patterns based on human expertise). The detailed prompt template is as follows:

Prompt template for Gemini Vision Pro and GPT-4 Vision

Variables:
 !<INPUT 0>! – Input type
 !<INPUT 1>! – Input Description Prompt
 !<INPUT 2>! – Normal Image
 !<INPUT 3>! – Anomaly Image

<commentblockmarker></commentblockmarker>
 The first image given about the !<INPUT 0>! is normal.

Please determine whether the second image given about the !<INPUT 0>! contains anomalies or defects. If yes, give a specific reason. Normally, the image given should depict clear and identifiable !<INPUT 0>! It may have defects such as broken parts, and contaminations.

Your answer should contain 2 parts:

"reasoning": a string, that describes what you think about the given image; "correctness": an integer, 1 if there is no anomaly in the image, 0 if it is, no partial credit;

Output example: {"reasoning": a string, "correctness": integer, 1 or 0}

Your response must be a valid JSON string starting with and should contain nothing else because we will directly execute it in Python. No indent or "n" in json structure formatting is needed. No ““ or ““json is needed.

B.2 Missing-modality Based Methods

To demonstrate how our **RADAR** model outperforms missing-modality based methods, we conducted comparative experiments on **MIAD Bench** using M3DM as baseline, evaluating against CMDIAD [41], ShaSpec [44], VLMo [1], and GMC [33]. Below we briefly introduce these models:

CMDIAD [41]: Proposes a Cross-Modal Distillation framework for Industrial Anomaly Detection, enabling multimodal training with few-modal inference to handle incomplete modalities in real-world scenarios.

ShaSpec [44]: Devises a "Shared Specific Feature Modeling" method focused on learning shared and specific features across multimodal data to address missing modality representations.

VLMo [1]: Introduces a hybrid multimodal expert model that leverages both the Dual Encoder for image retrieval tasks and the Fusion Encoder for multimodal encoding.

GMC [33]: Devises a geometric multimodal contrastive learning approach to tackle the challenge of inherent heterogeneity in multimodal learning.

C Efficiency on Parameters

We have integrated HyperNetwork [17] to dynamically cater to tasks with fewer parameters, aiming for enhanced performance [22]. During the training of our modality-incomplete instruction, we leveraged prompt learning by freezing all parameters of the simple Multimodal Transformer, retaining only the MLP and fully connected layer for downstream task processing. Consequently, the number of parameters that our model **RADAR** requires to train

Table 9: Comparison of parameter efficiency.

Methods	# Trained params	Relative proportion
M3DM (Baseline) [45]	510,603K	100%
RADAR (Ours)	6,842K	1.34%

Algorithm 1: Robust modality-instructive fusing and detecting framework (RADAR)

```

Input: Multimodal dataset  $\tilde{\mathcal{D}} = \{\mathcal{D}^C, \mathcal{D}^{2D}, \mathcal{D}^{3D}\}$ 
Output: Anomaly score  $\tau$ , segmentation map  $Seg_m$ 
Stage I: Adaptive Instruction Fusion
for each sample  $(d_{pc}, d_{rgb}) \in \tilde{\mathcal{D}}$  do
  if 3D point cloud  $d_{pc}$  missing then
     $\tilde{x}^{m1} \leftarrow \text{ones\_tensor}$  // Pseudo 3D input
     $f_{pc} \leftarrow \text{MaskTransformer}(\tilde{x}^{m1})$ 
  else
     $f_{pc} \leftarrow \text{Point-MAE}(\text{FPS}(d_{pc}))$  // Feature extraction
  if 2D RGB  $d_{rgb}$  missing then
     $\tilde{x}^{m2} \leftarrow \text{ones\_image}$  // Pseudo 2D input
     $f_{rgb} \leftarrow \text{ViT}(\tilde{x}^{m2})$ 
  else
     $f_{rgb} \leftarrow \text{ViT}(d_{rgb})$  // Feature extraction
  // Modality-Incomplete instruction
  if both modalities complete then
     $I_m \leftarrow I_{com}$ 
  else if only 3D missing then
     $I_m \leftarrow I_{rgb}$ 
  else if only 2D missing then
     $I_m \leftarrow I_{pc}$ 
  // Adaptive parameter learning
   $\{W^{(n)}, B^{(n)}\} \leftarrow \text{HyperNetwork}(f_{pc}, f_{rgb})$ 
   $\hat{G} \leftarrow \text{Transformer}(\text{concat}(I_m, f_{pc}, f_{rgb}))$ 
Stage II: Double-Pseudo Hybrid Detection
for each fused feature  $\hat{G}$  do
  // Branch 1: Global reconstruction
   $(\hat{x}_{rgb}, \hat{x}_{pc}) \leftarrow \text{Decoder}(\hat{G})$ 
   $\mathcal{L}_{recon} \leftarrow \lambda_{rgb} \|\hat{x}_{rgb} - x_{rgb}\|^2 + \lambda_{pc} \|\hat{x}_{pc} - x_{pc}\|^2$ 
  // Branch 2: Local contrastive learning
   $\{g_i\} \leftarrow \text{PatchPooling}(\hat{G})$ 
   $\mathcal{L}_{contrast} \leftarrow \text{BCE}(\text{TopK}(R_{fs}, \{g_i\}))$ 
  // Repository-based detection
   $R_{pc} \leftarrow \text{Update}(f_{pc}), R_{rgb} \leftarrow \text{Update}(f_{rgb})$ 
   $\tau \leftarrow \text{MDM}(R_{pc}, R_{rgb}, R_{fs})$ 
   $Seg_m \leftarrow \text{OCSVM}(R_{pc}, R_{rgb}, R_{fs})$ 
return  $\tau, Seg_m$ 

```

is significantly reduced. As illustrated in the Tab. 9, in contrast to the 510M parameter count in the Unsupervised Feature Fusion (UFF) module of the Baseline model M3DM [45], our model only necessitates training 6,842K parameter counts, representing merely 1.34%. Nonetheless, our model's performance significantly exceeds that of the Baseline.

D RADAR Pipeline Pseudocode

In this section, we present the algorithmic pipeline of our proposed **RADAR** for modality-incomplete industrial anomaly detection. The framework operates through two core stages: **i) Adaptive Instruction Fusion** that dynamically handles missing modalities via

learnable instructions and HyperNetwork-based parameter adaptation. **ii) Double-Pseudo Hybrid Detection** that mitigates overfitting through joint reconstruction-contrastive optimization.

Below, we provide the pseudocode (Algorithm 1) that formalizes three key innovations: **i**) modality-incomplete instruction injection for conditional feature fusion, **ii**) adaptive dynamic layers for missing-modality robustness, and **iii**) repository-based anomaly scoring with MDM and OCSVM. The algorithm explicitly captures how **RADAR** processes both complete (2D+3D) and incomplete (2D-only/3D-only) samples while maintaining detection stability across all missing-rate scenarios defined in **MIIAD Bench**.

E Comprehensive Comparison with MIAD Methods

The comparative experimental results between our **RADAR** model and the additional MIAD methods mentioned in Section B are presented in Tab. 10, Tab. 11, and Tab. 12. In addition to expanded comparisons with more MIAD methods, we have supplemented the P-AUROC results (Tab. 11) missing from the main text.

These more comprehensive experimental results further validate our key claims in the main text: that MIAD represents a novel, challenging, and practical task, and that our proposed **RADAR** framework effectively enhances the performance of MIAD methods.

F Comprehensive Comparison with Missing-modality Based Methods

The extensive comparative experimental results between our **RADAR** model and the additional missing-modality based methods mentioned in Section 2 are systematically presented in Tab. 13, Tab. 14, and Tab. 15, comprehensively covering all key evaluation metrics including I-AUROC, P-AUROC, and AUPRO.

These more extensive experimental results further validate our claims in the main text: current advanced missing-modality based methods still struggle with MIAD challenges, while our proposed **RADAR** framework significantly outperforms these approaches.

G Quantitative Results of P-AUROC and AUPRO

Furthermore, Fig. 6 and Fig. 7 qualitatively demonstrate the performance trends of different models' P-AUROC and AUPRO metrics under various settings as modality missing rates increase. The results reveal phenomena consistent with those observed for I-AUROC in the main text: while current MIAD methods show decreasing P-AUROC and AUPRO scores with increasing modality missing rates, our **RADAR** method still achieves significant performance improvements over the baseline.

H Comprehensive Ablation Study

Tab. 16 presents more comprehensive ablation results, showing the relationship between model components and I-AUROC/AUPRO metrics under various modality missing scenarios: 30% PC, 50% PC, 70% PC, 30% RGB, 50% RGB, and 70% RGB missing rates.

The experimental results reconfirm that all three components in our framework effectively enhance baseline performance, with Modality-incomplete Instruction (MII) demonstrating the most

Table 10: I-AUROC score in performance comparison of different MIAD methods on *MIIAD Bench*. Red bold values indicate the best experimental performance, while underlined values denote the second-best results.

Missing Rate	MIIAD Bench Split	Data in # Train		Data in # Test		I-AUROC							
		3D PC	2D RGB	3D PC	2D RGB	Gemini-V	GPT-4V	BTF [19]	AST [38]	AnomalyGPT [14]	M3DM [45]	Shape-Guided [8]	RADAR (Ours)
0%	MVTec-3D AD	100%		100%		0.574	0.753	0.865	0.937	0.922	0.945	0.947	0.947
	Eycandies	100%		100%		0.503	0.676	0.816	0.879	0.857	<u>0.897</u>	0.891	0.901
30%	MVTec-3D AD	100%	70%	100%	70%	0.521	0.682	0.813	0.869	0.841	0.892	0.910	0.908
		70%	100%	70%	100%	0.506	0.693	0.795	<u>0.901</u>	0.828	0.883	0.869	0.903
		85%	85%	85%	85%	0.515	0.684	0.797	0.873	0.826	<u>0.886</u>	0.883	0.907
	Eye-candies	100%	70%	100%	70%	0.462	0.624	0.749	0.826	0.784	0.844	<u>0.864</u>	0.869
50%	MVTec-3D AD	100%	50%	100%	50%	0.446	0.591	0.736	0.772	0.732	0.796	0.811	0.810
		50%	100%	50%	100%	0.459	0.584	0.718	<u>0.807</u>	0.724	0.789	0.773	0.821
		75%	75%	75%	75%	0.450	0.587	0.726	0.782	0.718	0.791	<u>0.799</u>	0.817
	Eye-candies	100%	50%	100%	50%	0.414	0.565	0.685	0.742	0.703	0.765	<u>0.786</u>	0.795
70%	MVTec-3D AD	100%	30%	100%	30%	0.316	0.476	0.606	0.653	0.616	0.675	<u>0.685</u>	0.707
		30%	100%	30%	100%	0.332	0.488	0.588	<u>0.671</u>	0.608	0.662	0.649	0.703
		65%	65%	65%	65%	0.324	0.484	0.594	0.660	0.615	0.668	<u>0.672</u>	0.706
	Eye-candies	100%	30%	100%	30%	0.284	0.437	0.563	0.601	0.571	0.629	<u>0.635</u>	0.662
		30%	100%	30%	100%	0.271	0.429	0.552	<u>0.624</u>	0.565	0.623	0.611	0.654
		65%	65%	65%	65%	0.279	0.433	0.559	0.614	0.570	0.624	<u>0.626</u>	0.658

Table 11: P-AUROC score in performance comparison of different MIAD methods on *MIIAD Bench*.

Missing Rate	MIIAD Bench Split	Data in # Train		Data in # Test		P-AUROC							
		3D PC	2D RGB	3D PC	2D RGB	Gemini-V	GPT-4V	BTF [19]	AST [38]	AnomalyGPT [14]	M3DM [45]	Shape-Guided [8]	RADAR (Ours)
0%	MVTec-3D AD	100%		100%		0.606	0.787	0.992	0.976	0.927	0.992	0.985	0.992
	Eycandies	100%		100%		0.575	0.754	0.981	0.958	0.906	0.977	0.979	0.981
30%	MVTec-3D AD	100%	70%	100%	70%	0.526	0.722	0.945	0.916	0.857	0.945	0.930	0.955
		70%	100%	70%	100%	0.518	0.715	<u>0.941</u>	0.909	0.849	0.938	0.923	0.948
		85%	85%	85%	85%	0.532	0.728	0.942	0.913	0.861	<u>0.947</u>	0.928	0.953
	Eye-candies	100%	70%	100%	70%	0.495	0.694	<u>0.933</u>	0.898	0.836	0.928	0.919	0.943
50%	MVTec-3D AD	100%	50%	100%	50%	0.441	0.632	0.865	0.826	0.767	<u>0.868</u>	0.850	0.888
		50%	100%	50%	100%	0.433	0.625	<u>0.863</u>	0.818	0.759	0.857	0.842	0.880
		75%	75%	75%	75%	0.447	0.638	0.860	0.823	0.771	<u>0.861</u>	0.848	0.885
	Eye-candies	100%	50%	100%	50%	0.412	0.604	<u>0.853</u>	0.808	0.746	0.847	0.839	0.873
70%	MVTec-3D AD	100%	30%	100%	30%	0.351	0.532	0.744	0.716	0.657	<u>0.755</u>	0.740	0.785
		30%	100%	30%	100%	0.343	0.525	<u>0.747</u>	0.708	0.649	0.741	0.732	0.777
		65%	65%	65%	65%	0.357	0.538	0.751	0.713	0.661	<u>0.755</u>	0.738	0.782
	Eye-candies	100%	30%	100%	30%	0.327	0.504	<u>0.743</u>	0.698	0.636	0.737	0.729	0.763
		30%	100%	30%	100%	0.319	0.497	<u>0.735</u>	0.690	0.628	0.729	0.721	0.755
		65%	65%	65%	65%	0.333	0.510	<u>0.739</u>	0.695	0.641	0.733	0.726	0.760

significant impact, followed by Double-Pseudo Hybrid Module (DPHM), and finally Adaptive Learning Module (ALM).

I Ablation Study of Double-Branch

The ablation study on dual-branch architecture (Tab. 17) reveals several key insights. When implemented individually, both branches demonstrate measurable performance gains over the baseline, with Branch 2 showing slightly stronger results in point cloud missing scenarios (0.888 vs 0.886 at 30% PC) while Branch 1 performs

marginally better in RGB missing conditions (0.684 vs 0.683 at 70% RGB). This suggests specialized feature extraction capabilities: Branch 2 appears more sensitive to geometric information while Branch 1 better captures texture patterns.

Significantly greater improvements emerge when integrating each branch with complementary modules. The addition of Branch 1 boosts performance by 1.6 – 3.1% across test conditions, while Branch 2 delivers even stronger gains of 1.8 – 3.5%. However, the

Table 12: AUPRO score in performance comparison of different MIAD methods on *MIIAD Bench*.

Missing Rate	MIIAD Bench Split	Data in # Train		Data in # Test		AUPRO					
		3D PC	2D RGB	3D PC	2D RGB	Gemini-V	GPT-4V	BTF [19]	M3DM [45]	Shape-Guided [8]	RADAR (Ours)
0%	MVTec-3D AD	100%		100%		0.344	0.572	0.959	0.964	0.976	0.967
	Eyecandies	100%		100%		0.297	0.514	0.866	<u>0.882</u>	0.876	0.885
30%	MVTec-3D AD	100%	70%	100%	70%	0.315	0.544	0.903	0.911	<u>0.924</u>	0.925
		70%	100%	70%	100%	0.307	0.530	<u>0.937</u>	0.932	0.918	0.947
		85%	85%	85%	85%	0.309	0.540	0.914	0.917	<u>0.923</u>	0.929
	Eye-candies	100%	70%	100%	70%	0.264	0.453	0.813	<u>0.828</u>	0.832	0.847
		70%	100%	70%	100%	0.248	0.458	<u>0.846</u>	0.832	0.829	0.851
		85%	85%	85%	85%	0.252	0.454	0.821	0.830	<u>0.831</u>	0.854
50%	MVTec-3D AD	100%	50%	100%	50%	0.248	0.485	0.826	0.835	<u>0.848</u>	0.857
		50%	100%	50%	100%	0.261	0.489	<u>0.857</u>	0.849	0.838	0.874
		75%	75%	75%	75%	0.253	0.483	0.819	<u>0.833</u>	0.831	0.862
	Eye-candies	100%	50%	100%	50%	0.202	0.387	0.731	<u>0.749</u>	0.746	0.772
		50%	100%	50%	100%	0.206	0.375	<u>0.750</u>	0.741	0.741	0.769
		75%	75%	75%	75%	0.212	0.380	<u>0.744</u>	0.742	0.738	0.771
70%	MVTec-3D AD	100%	30%	100%	30%	0.183	0.394	0.702	0.715	<u>0.729</u>	0.755
		30%	100%	30%	100%	0.184	0.401	<u>0.718</u>	0.709	0.696	0.748
		65%	65%	65%	65%	0.178	0.398	0.706	0.711	<u>0.714</u>	0.752
	Eye-candies	100%	30%	100%	30%	0.154	0.334	0.596	0.613	<u>0.616</u>	0.647
		30%	100%	30%	100%	0.162	0.328	<u>0.619</u>	0.608	0.602	0.649
		65%	65%	65%	65%	0.159	0.331	0.601	0.610	<u>0.615</u>	0.649

Table 13: I-AUROC score in performance comparison of missing-modality based methods on *MIIAD Bench*.

Missing Rate	MIIAD Bench Split	Data in # Train		Data in # Test		I-AUROC					
		3D PC	2D RGB	3D PC	2D RGB	M3DM (Baseline) [45]	+GMC [33]	+VLMo [1]	+ShaSpec [44]	+CMDIAD [41]	+RADAR (Ours)
0%	MVTec-3D AD	100%		100%		0.945	0.931	0.937	0.943	0.948	0.947
	Eyecandies	100%		100%		0.897	0.886	0.897	0.891	<u>0.898</u>	0.901
30%	MVTec-3D AD	100%	70%	100%	70%	0.892	0.878	0.895	<u>0.901</u>	0.898	0.908
		70%	100%	70%	100%	0.883	0.868	0.888	0.887	<u>0.894</u>	0.903
		85%	85%	85%	85%	0.886	0.872	0.892	0.893	<u>0.897</u>	0.907
	Eye-candies	100%	70%	100%	70%	0.844	0.830	<u>0.848</u>	0.847	0.842	0.869
		70%	100%	70%	100%	0.843	0.828	0.842	<u>0.851</u>	0.845	0.858
		85%	85%	85%	85%	0.843	0.829	0.844	<u>0.852</u>	0.843	0.867
50%	MVTec-3D AD	100%	50%	100%	50%	0.796	0.776	0.792	<u>0.803</u>	0.801	0.810
		50%	100%	50%	100%	0.789	0.770	0.787	<u>0.797</u>	0.795	0.821
		75%	75%	75%	75%	0.791	0.771	0.789	<u>0.798</u>	0.797	0.817
	Eye-candies	100%	50%	100%	50%	0.765	0.745	0.763	<u>0.772</u>	0.770	0.795
		50%	100%	50%	100%	0.757	0.737	0.755	<u>0.764</u>	0.762	0.780
		75%	75%	75%	75%	0.759	0.739	0.757	<u>0.766</u>	0.764	0.787
70%	MVTec-3D AD	100%	30%	100%	30%	0.675	0.655	<u>0.680</u>	0.679	0.654	0.707
		30%	100%	30%	100%	0.662	0.642	0.664	<u>0.671</u>	0.652	0.703
		65%	65%	65%	65%	0.668	0.648	0.672	<u>0.677</u>	0.653	0.706
	Eye-candies	100%	30%	100%	30%	0.629	0.610	0.621	<u>0.634</u>	0.615	0.662
		30%	100%	30%	100%	0.623	0.604	0.616	<u>0.624</u>	0.607	0.654
		65%	65%	65%	65%	0.624	0.605	0.617	<u>0.626</u>	0.610	0.658

full integration of both branches with all modules achieves optimal results, particularly excelling under challenging 70% missing rates with 4.1% improvement for point cloud and 4.0% for RGB modalities. This demonstrates that while each branch contributes valuable representations, their synergistic combination is essential

for maximal performance, confirming the architectural design's effectiveness in handling multimodal missing data scenarios.

Table 14: P-AUROC score in performance comparison of missing-modality based methods on *MIIAD Bench*.

Missing Rate	MIIAD Bench Split	Data in # Train		Data in # Test		P-AUROC					
		3D PC	2D RGB	3D PC	2D RGB	M3DM (Baseline) [45]	+GMC [33]	+VLMo [1]	+ShaSpec [44]	+CMDIAD [41]	+RADAR (Ours)
0%	MVTec-3D AD	100%		100%		0.992	0.977	0.991	0.992	0.991	0.992
	Eyecandies	100%		100%		0.977	0.962	0.976	<u>0.978</u>	0.977	0.981
30%	MVTec-3D AD	100%	70%	100%	70%	0.945	0.929	0.943	<u>0.949</u>	0.947	0.955
		70%	100%	70%	100%	0.938	0.922	0.936	<u>0.941</u>	0.939	0.948
		85%	85%	85%	85%	0.942	0.926	0.940	<u>0.945</u>	0.943	0.953
	Eye-candies	100%	70%	100%	70%	0.928	0.912	0.926	<u>0.933</u>	0.930	0.943
		70%	100%	70%	100%	0.921	0.905	0.919	<u>0.926</u>	0.923	0.936
		85%	85%	85%	85%	0.925	0.909	0.923	<u>0.930</u>	0.927	0.941
50%	MVTec-3D AD	100%	50%	100%	50%	0.865	0.849	0.863	<u>0.872</u>	0.870	0.888
		50%	100%	50%	100%	0.857	0.841	0.855	<u>0.864</u>	0.862	0.880
		75%	75%	75%	75%	0.861	0.845	0.859	<u>0.868</u>	0.866	0.885
	Eye-candies	100%	50%	100%	50%	0.847	0.831	0.845	<u>0.853</u>	0.851	0.873
		50%	100%	50%	100%	0.839	0.823	0.837	<u>0.845</u>	0.843	0.865
		75%	75%	75%	75%	0.843	0.827	0.841	<u>0.849</u>	0.847	0.870
70%	MVTec-3D AD	100%	30%	100%	30%	0.755	0.740	0.753	<u>0.760</u>	0.758	0.785
		30%	100%	30%	100%	0.747	0.732	0.745	<u>0.752</u>	0.750	0.777
		65%	65%	65%	65%	0.751	0.736	0.749	<u>0.756</u>	0.754	0.782
	Eye-candies	100%	30%	100%	30%	0.737	0.722	0.735	<u>0.742</u>	0.740	0.763
		30%	100%	30%	100%	0.729	0.714	0.727	<u>0.734</u>	0.732	0.755
		65%	65%	65%	65%	0.733	0.718	0.731	<u>0.738</u>	0.736	0.760

Table 15: AUPRO score in performance comparison of missing-modality based methods on *MIIAD Bench*.

Missing Rate	MIIAD Bench Split	Data in # Train		Data in # Test		AUPRO					
		3D PC	2D RGB	3D PC	2D RGB	M3DM (Baseline) [45]	+GMC [33]	+VLMo [1]	+ShaSpec [44]	+CMDIAD [41]	+RADAR (Ours)
0%	MVTec-3D AD	100%		100%		0.964	0.952	<u>0.965</u>	0.958	0.960	0.967
	Eyecandies	100%		100%		0.882	0.871	0.883	0.882	<u>0.884</u>	0.885
30%	MVTec-3D AD	100%	70%	100%	70%	0.911	0.895	0.910	<u>0.915</u>	0.911	0.925
		70%	100%	70%	100%	0.932	0.915	0.934	<u>0.938</u>	0.916	0.947
		85%	85%	85%	85%	0.917	0.902	<u>0.918</u>	0.917	0.913	0.929
	Eye-candies	100%	70%	100%	70%	0.828	0.813	0.827	<u>0.834</u>	0.831	0.847
		70%	100%	70%	100%	0.832	0.817	0.835	<u>0.841</u>	0.838	0.851
		85%	85%	85%	85%	0.830	0.815	0.833	<u>0.840</u>	0.835	0.854
50%	MVTec-3D AD	100%	50%	100%	50%	0.835	0.817	0.833	<u>0.843</u>	0.840	0.857
		50%	100%	50%	100%	0.849	0.831	0.847	<u>0.856</u>	0.854	0.874
		75%	75%	75%	75%	0.833	0.815	0.830	<u>0.839</u>	0.837	0.862
	Eye-candies	100%	50%	100%	50%	0.749	0.734	0.746	<u>0.755</u>	0.753	0.772
		50%	100%	50%	100%	0.741	0.726	0.738	<u>0.748</u>	0.746	0.769
		75%	75%	75%	75%	0.742	0.727	0.739	<u>0.749</u>	0.747	0.771
70%	MVTec-3D AD	100%	30%	100%	30%	0.715	0.703	0.710	<u>0.717</u>	0.703	0.755
		30%	100%	30%	100%	0.709	0.708	0.713	<u>0.718</u>	0.712	0.748
		65%	65%	65%	65%	0.711	0.701	0.711	<u>0.717</u>	0.707	0.752
	Eye-candies	100%	30%	100%	30%	0.613	0.597	0.611	<u>0.614</u>	0.606	0.647
		30%	100%	30%	100%	0.608	0.592	0.605	<u>0.611</u>	0.598	0.649
		65%	65%	65%	65%	0.610	0.598	0.608	<u>0.613</u>	0.601	0.649

J Ablation Study of Hyper-Parameters

To systematically analyze the impact of λ_{rgb} and λ_{pc} in the reconstruction loss of Stage2 Branch 1, we conduct controlled experiments with seven parameter configurations under varying point cloud (PC) missing rates (30%, 50%, 70%). The experimental setup

includes: (1) *Baseline* without weight adjustment ($\lambda_{rgb} = 0$, $\lambda_{pc} = 0$), (2) 3D-only weighting ($\lambda_{rgb} = 0$, $\lambda_{pc} = 0.5$), (3) RGB-only emphasis ($\lambda_{rgb} = 1.0$, $\lambda_{pc} = 0$), (4) Balanced weights ($\lambda_{rgb} = 0.7$, $\lambda_{pc} = 0.3$),

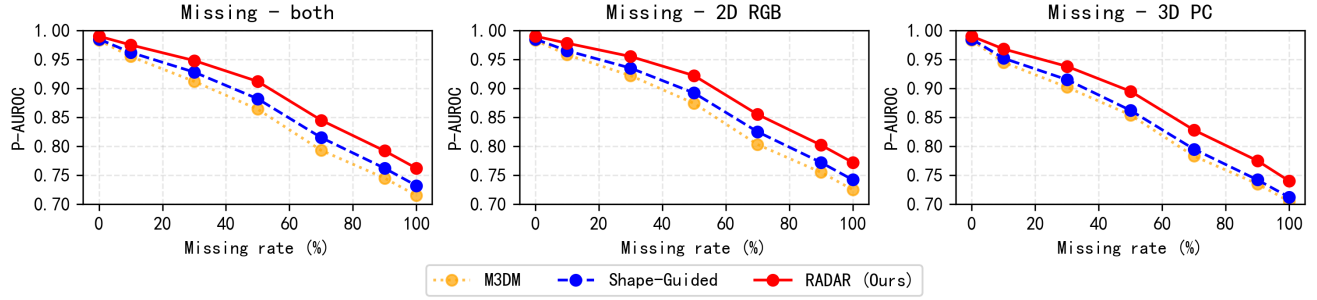


Figure 6: Quantitative results of P-AUROC on the *MIIAD Bench* - MVTEC-3D AD with different missing rates under different missing-modality scenarios. Each data point in the figure represents that training and testing are with the same $\eta\%$ missing rate.

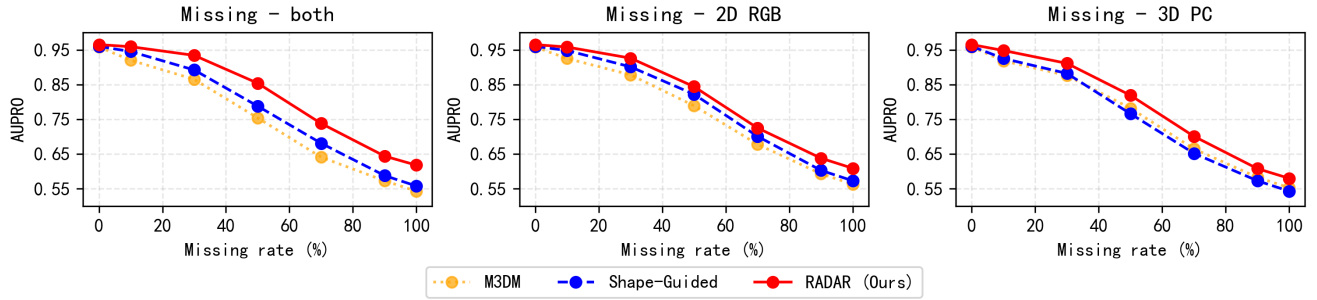


Figure 7: Quantitative results of AUPRO on the *MIIAD Bench* - MVTEC-3D AD with different missing rates under different missing-modality scenarios. Each data point in the figure represents that training and testing are with the same $\eta\%$ missing rate.

Table 16: Ablation study of different modules under varying missing rates on *MIIAD Bench* - MVTEC-3D AD. Here I-A. represents I-AUROC, AUP. represents AUPRO.

Methods	Setting			30% PC		50% PC		70% PC		30% RGB		50% RGB		70% RGB	
	MII	ALM	DPHM	I-A.	AUP.										
Baseline				0.883	0.932	0.789	0.849	0.662	0.709	0.892	0.911	0.796	0.835	0.675	0.715
+ MII	✓			0.892	0.940	0.802	0.860	0.680	0.725	0.899	0.918	0.808	0.845	0.690	0.728
+ ALM		✓		0.885	0.934	0.795	0.853	0.668	0.714	0.893	0.914	0.801	0.839	0.683	0.721
+ DPHM			✓	0.889	0.937	0.798	0.856	0.675	0.719	0.896	0.917	0.805	0.842	0.687	0.725
+ MII & ALM	✓	✓		0.898	0.943	0.810	0.865	0.688	0.732	0.905	0.923	0.816	0.851	0.698	0.736
+ MII & DPHM	✓		✓	0.902	0.945	0.816	0.868	0.693	0.738	0.907	0.925	0.823	0.858	0.705	0.743
+ ALM & DPHM		✓	✓	0.894	0.940	0.804	0.862	0.682	0.727	0.901	0.921	0.810	0.848	0.693	0.733
RADAR (Ours)	✓	✓	✓	0.903	0.947	0.821	0.874	0.703	0.748	0.908	0.925	0.830	0.865	0.715	0.755

Table 17: Ablation study of dual-branch architecture on *MIIAD Bench* - MVTEC-3D AD. Performance reported in I-AUROC. Here “others” represents other modules.

Configurations	30% PC	70% PC	30% RGB	70% RGB
Baseline	0.883	0.662	0.892	0.675
w Branch 1 (only)	0.886	0.670	0.894	0.684
w Branch 2 (only)	0.888	0.671	0.894	0.683
w Branch 1 + others	0.899	0.693	0.905	0.706
w Branch 2 + others	0.901	0.698	0.907	0.710
All modules (Ours)	0.903	0.703	0.908	0.715

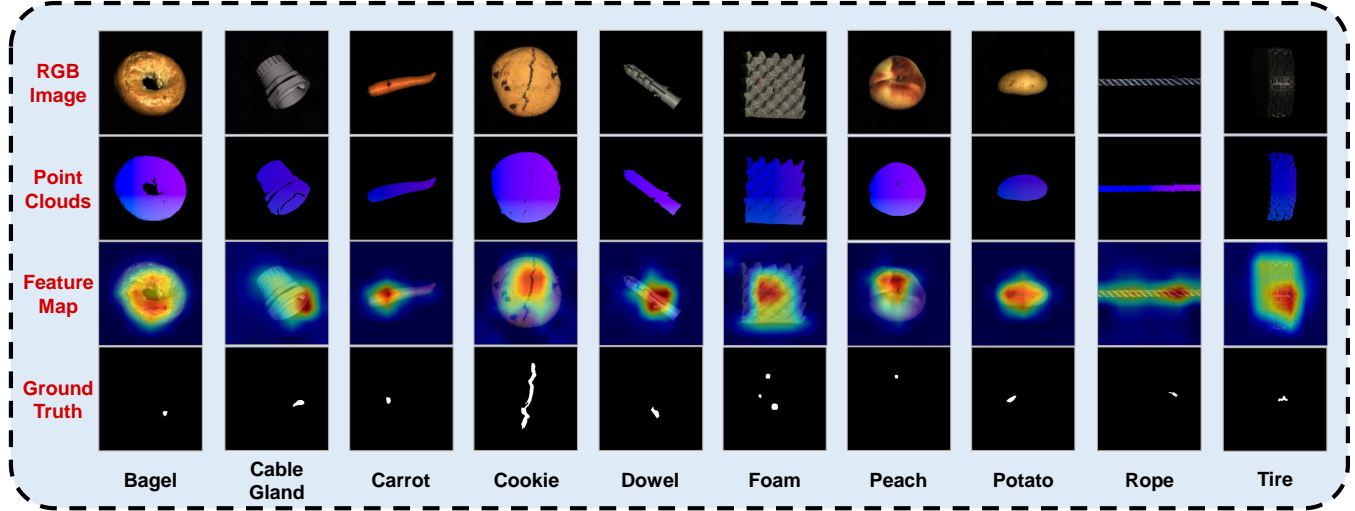


Figure 8: Additional visualization results of industrial anomaly detection.

Table 18: Ablation study of λ parameters on *MIIAD Bench* - MVtec-3D AD. Here I-A. represents I-AUROC, AUP. represents AUPRO.

Configurations	Parameters		30% PC		50% PC		70% PC	
	λ_{rgb}	λ_{pc}	I-A.	AUP.	I-A.	AUP.	I-A.	AUP.
Baseline	0.0	0.0	0.898	0.943	0.810	0.865	0.688	0.732
λ_{pc} Only	0.0	0.5	0.894	0.939	0.804	0.858	0.679	0.724
λ_{rgb} Only	1.0	0.0	0.897	0.942	0.805	0.859	0.683	0.726
Balanced	0.7	0.3	0.899	0.945	0.812	0.863	0.691	0.734
Mixed	1.0	0.3	<u>0.901</u>	0.947	<u>0.816</u>	<u>0.867</u>	<u>0.697</u>	<u>0.739</u>
Optimal (Ours)	1.0	0.5	0.903	0.947	0.821	0.874	0.703	0.748
Overweight PC	0.5	1.0	0.895	0.940	0.807	0.858	0.685	0.729

(5) Asymmetric combination ($\lambda_{rgb} = 1.0, \lambda_{pc} = 0.3$), (6) Our optimal configuration ($\lambda_{rgb} = 1.0, \lambda_{pc} = 0.5$), and (7) 3D-overweighted scenario ($\lambda_{rgb} = 0.5, \lambda_{pc} = 1.0$).

Experimental results are shown in Tab. 18, which reveal that the optimal configuration ($\lambda_{rgb} = 1.0 + \lambda_{pc} = 0.5$) achieves consistent performance gains across all test conditions, with I-AUROC improvements of +1.1% (50% PC missing rate) and +1.5% (70% PC missing rate) compared to baseline.

Notably, the λ_{rgb} -only configuration shows better robustness than λ_{pc} -only at 30% missing rate (+0.3% I-AUROC, 0.897 vs 0.894), indicating RGB modality's stronger discriminative power in partial observation scenarios. However, both single-modality configurations underperform the baseline, demonstrating the necessity of multimodal integration.

The synergistic effect of combined weights yields maximum performance, where 3D weighting provides complementary geometric constraints without overriding RGB's texture sensitivity. The performance degradation in 3D-overweighted configuration (−0.3% I-AUROC at 70% missing rate compared to baseline) further validates the importance of maintaining modality balance.

K Additional Visualization Results

As depicted in Fig. 8, we present additional industrial anomaly results for all categories within the MIIAD Dataset. As can be seen from the figure, for each category of the dataset, our model can identify abnormal industrial entities while accurately locating the position of anomalies.